Dissociative recombination of CH^+: Cross section and final states

Z. Amitay and D. Zajfman
Department of Particle Physics, Weizmann Institute of Science, Rehovot, 76100, Israel

P. Forck,* U. Hechtfischer, B. Seidel, M. Grieser, D. Habs, R. Repnow, D. Schwalm, and A. Wolf
Max-Planck-Institut für Kernphysik and Physikalisches Institut der Universität Heidelberg, D-69029 Heidelberg, Germany
(Received 10 May 1996)

The cross section as well as the branching ratios for the dissociative recombination of ground-state CH^+ ions with electrons have been measured using the heavy-ion storage-ring technique and two-dimensional fragment imaging. Although the absolute value of the cross section at thermal energies is found to be in very good agreement with the theory, several unpredicted narrow resonances are also present in the data. These structures are interpreted as due to an indirect recombination process via core-excited Rydberg states. The branching-ratio measurement shows that at low electron energy the $2\,^2\Pi$ state, producing carbon fragments $C(^1D)$, is the most important dissociative state, although transitions during the dissociation to other dissociative potential curves are also present. Anisotropy in the angular distribution of the dissociating fragments is visible for some of the final states. Dissociative recombination of ions in the metastable excited $a\,^3\Pi$ state is also observed, and the lifetime as well as the excitation energy of this state are deduced from the imaging data. [S1050-2947(96)00111-4]

PACS number(s): 34.80.Lx

I. INTRODUCTION

Dissociative recombination (DR) of molecular ions with electrons is a process of great significance to the physics of laboratory and astrophysical plasmas [1]. It is a collision process which starts by the binding of an electron to a molecular ion and proceeds via a mechanism in which the resulting electron-ion compound dissociates into neutral fragments. During the recombination, the electron kinetic energy E is absorbed by the molecule and in the dissociation, excess energy is carried away in the form of kinetic and internal energy of the fragments. For CH^+, the DR process can be represented as

$$CH^+(v)+e^-(E)\rightarrow C(nl)+H(n'l'), \qquad (1)$$

where v denotes the initial vibrational quantum state of CH^+, and nl and $n'l'$ are the principal and angular quantum numbers for the C and H fragments, respectively. CH^+ plays a key role in the chemistry of cosmic and planetary molecular clouds [2]; in particular, the DR of CH^+ is a major process in the chain of destruction-production of this molecular ion, which has been found in overabundance in interstellar clouds [3] when compared to standard interstellar chemistry models. These models are heavily based on absolute cross sections for the formation and destruction of molecular species, so that the DR cross section of CH^+ is of wider interest. It is important to consider that, as in general the temperatures of interstellar clouds are low ($T\leqslant 100$ K), the main contribution to the DR of CH^+ comes from ions in their vibrational and electronic ground state ($X\,^1\Sigma^+$, $v=0$).

On the theoretical side, the DR of even the simplest molecular ions is not yet completely understood and far from being precisely modeled. Although it was described more than 40 years ago by Bates [4] as a dissociation due to the crossing between an excited neutral dissociative state and the bound ionic ground state close to its minimum, new mechanisms for the recombination and dissociation have been found during the following years, including recently recombination without curve crossing [5]. The basic theories of DR always calculate the cross section for a given collision energy E from a single initial (rovibrational) state (v,J) of the molecular ion to a set of final (electronic) states of the neutral fragments. For the vibrational ground state of CH^+, only a few theoretical DR calculations have been done. Bardsley and Junker [6] and Krauss and Julienne [7] theoretically estimated the dissociative recombination rate to be about 10^{-7} $cm^3\,s^{-1}$ at $T=100$ K. They carried out a configuration mixing calculation of adiabatic potentials and found that the $2\,^2\Pi$ dissociative potential curve of CH crosses the lowest potential curve of the ion close to its equilibrium internuclear distance. A few years later Giusti-Suzor and Lefebvre-Brion [8], again using a configuration mixing calculation but including the diffuse Rydberg character of the dissociative electronic state, concluded that this state does *not* cross with the ionic state. Accordingly, the rate was conjectured to be smaller by two orders of magnitude than the former theoretical estimates. Further calculations by van Dishoeck [9] (configuration mixing) and Tennyson [10] (R matrix) left the crucial curve crossing problem unsolved. The most recent and complete calculation for the DR of CH^+ was carried out by Takagi, Kosugi, and Le Dourneuf [11] using multichannel quantum defect theory. The dissociative state was found to cross the lowest potential of CH^+ near the left turning point of the first excited vibrational state. The rate constant obtained was 1.12×10^{-7} $cm^3\,s^{-1}$ at $T=120$ K. This calculation predicts an overall cross-section dependence over the elec-

*Present address: Gesellschaft für Schwerionenforschung (GSI), D-64220 Darmstadt, Germany.

tron energy which is steeper than $\sigma \propto E^{-1}$ for the energy range $E<0.3$ eV. Many Rydberg resonances associated with vibrational excitations of the ionic core, giving rise to the so-called indirect process [12], are present in the cross section.

On the experimental side, the DR of molecular ions has been studied using various methods [1]. Among them, the merged-beam method [13] is the most versatile one as it permits a high sensitivity and a fine control over the collision energy. In the merged-beam configuration, a fast molecular-ion beam is created in the ion source of an accelerator and after collimation is merged with a cold electron beam, where the beams are collinear and the recombination takes place. The rate of neutralization is recorded as a function of the relative electron–molecular-ion energy (E) and the cross section is extracted after proper normalization. One of the main drawbacks of this method is related to the uncertainty of the initial vibrational and rotational states' distribution: As the molecular ions are usually created by the ionization of the parent neutral molecule or by dissociation and ionization of a neutral gas, the ions may be found in a wide distribution of vibrational states. Therefore, since DR often is very sensitive to the initial vibrational state (the sensitivity to the initial rotational state is still subject to discussion), the extracted cross section cannot be directly compared to the theoretical calculation. Mul *et al.* [14] have measured the DR of CH^+ using the merged-beam method. Although a variety of buffer gases were used in their ion source in order to quench the vibrational excitation, as well as the $a\ ^3\Pi$ electronic metastable state, it is not clear that the measured DR cross section represents that of fully relaxed CH^+. In this measurement, the cross section was found to decrease as E^{-1}, i.e., slower than the theoretical prediction [11]. Its absolute value at low energy was found to be about a factor of 2 higher than the theoretical value.

During the last few years there has been substantial progress in the ability to measure DR under controlled conditions. This has been achieved with the help of the heavy-ion storage-ring technique, which allows one to store fast molecular-ion beams for a time long enough to allow for complete deexcitation of initial electronic and vibrational excitations via spontaneous radiative transitions, and then to merge the internally cold molecular-ion beam with an intense electron beam (using the electron cooler of the storage ring). Thus the advantages of the merged-beam arrangement (i.e., high sensitivity and tunability) are conserved and, in addition, the molecular ions are known to be in the ground vibrational states ($v=0$). On the other hand, the present storage-ring technique does not yet provide information on the rotational distribution of states, since rotational cooling is much slower than vibrational cooling [15] and is limited by the ambient temperature of the storage ring (300 K). However, progress towards a better diagnostic of the rotational population is currently underway [16]. Using the heavy-ion storage-ring technique, relative as well as absolute DR cross sections have been measured for various molecules [17–19], among them also CD^+ [20], and unknown features have been discovered.

The next step toward a detailed comparison between the theoretical and experimental DR of a specific molecular ion is the measurement of the final electronic states of the neutralized atomic fragments. A complete measurement of such branching ratios has recently been published for HD^+ [21] using the technique of two-dimensional fragment imaging, and has provided very detailed information concerning the DR mechanisms of HD^+. Hence using the storage-ring technique to provide well-defined initial conditions for the molecular ions, and the imaging technique to yield information on the final states of the fragments, it becomes possible to perform a *state by state* direct comparison with theoretical calculations. Besides the importance of such experimental data for the basic understanding of the DR process, the information on final-state branching ratios also has significant implications for astrophysical chemistry, atmospheric modeling, and laboratory plasma physics [1].

In the present work we have measured the absolute cross section for the DR of vibrationally cold CH^+ using the heavy-ion storage-ring technique and also determined a complete set of branching ratios for the different final electronic states of the carbon and hydrogen fragments at various incident electron energies. Section II of this paper describes the experimental technique for measuring the absolute cross section as well as the final states using the fragment imaging technique. In Sec. III experimental results are presented both for the absolute cross section and for the branching ratios. A discussion and the comparison with theoretical and previous experimental data are presented in Sec. IV. We also present a measurement of the DR cross section for CD^+ ions. Measurements on this ion were already published [20] but have been repeated with improved energy resolution in the present work.

II. EXPERIMENTAL PROCEDURE

A. General experimental setup

The present experiment was carried out at the heavy-ion test storage ring (TSR) located at the Max-Planck-Institut für Kernphysik, Heidelberg, Germany [22]. Negative molecular ions CH^- were produced from a standard Cs sputter source filled with CH_4 and equipped with a carbon target, and were accelerated toward the high-voltage terminal of a tandem accelerator. Upon reaching the terminal, the CH^- ions were stripped using a thin gas target and the resulting CH^+ beam was accelerated up to 7.2 MeV and injected into the TSR. After each injection, typically 10^6 particles circulated in the ring (nominal circumference 55.4 m) in a (ring-averaged) vacuum of 7×10^{-11} mbar (absolute pressure with more than 90% H_2) with a beam lifetime of 10 s, allowing statistically significant measurements up to 25 s after the injection. The CD^+ beam was produced from the same ion source, except that it was filled with CD_4, the injection energy was 6.6 MeV, and the lifetime after injection was only 4.6 s, due to a somewhat higher average pressure in the TSR during the CD^+ beam time.

At each turn, the ion beam was merged with the 5.0-cm-diam electron beam of the electron cooler over a length of nominally 1.5 m. This arrangement of merged beams in a storage ring is also used for measuring dielectronic recombination cross sections of highly charged ions and the general conditions and procedures of such measurements have been described in more detail elsewhere [23]. Basically, the collision energy between electrons and ions is varied by tuning

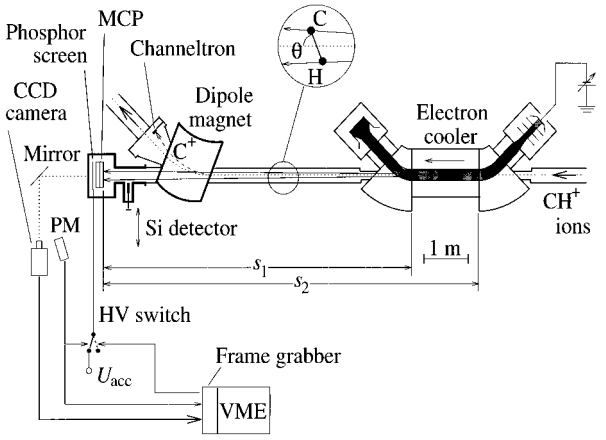

FIG. 1. Experimental setup for the measurement of the DR cross section of CH^+ and CD^+. The MCP detector (together with its phosphor screen) and the Si detector are located in a vacuum chamber following the first dipole magnet after the electron-ion interaction region. Positions of impact of neutral C and H (or D) fragments are read via a mirror by a CCD camera coupled to a high speed frame grabber located in a VME (Versa Module Europa) crate. The photomultiplier (PM) is used for shutting off the acceleration voltage (U_{acc}) between the phosphor screen and the channel plate, as discussed in the text. The detector setup is shown not to scale.

the electron beam energy while keeping the energy of the stored ions at fixed value. In the present experiment, typical values for the electron beam energy and current at low collision energy (i.e., closely matched electron and ion beam velocities) were 300 eV and 5.5 mA, respectively, corresponding to an electron density of 1.7×10^6 cm^{-3}. In the interaction region, the electrons were guided by a 33-mT longitudinal magnetic field. In order to reach the best possible collision-energy resolution, the electron beam was magnetically expanded before entering the interaction region to reduce its transverse energy spread [24]. The thermal electron energies in the comoving frame of the electron beam amount to $kT_\perp=17$ meV for the transverse degrees of freedom after the magnetic expansion and to $kT_\parallel\approx0.5$ meV for the longitudinal degree of freedom.

After each injection, the molecular ions were first electron cooled for 6 s in order to ensure equal velocity of the ion and electron beams. After this cooling period, measurements on the DR of CH^+ (CD^+) are performed by detecting the neutral fragments C and H (D) produced in the interaction region, using a detector mounted straight ahead of the cooler at a distance of ≈6 m (see Fig. 1). Two different types of detectors were installed for these molecular measurements: an energy-sensitive detector for measuring the absolute cross section, and a two-dimensional imaging detector for the final-state measurement. The energy-sensitive detector was movable and located in front of the imaging detector so that the detectors could be interchanged without breaking the vacuum.

The adjustment of the electron cooler, in particular the relative alignment of the electron and the ion beams, was facilitated by using a pilot beam of higher intensity than the molecular-ion beam, having the same magnetic rigidity and similar velocity ($^{13}C^+$ for the CH^+ beam time and $^{28}Si^{2+}$ for the CD^+ beam time). By observing and optimizing the transverse cooling of the pilot beam, the collinearity of the electron and the ion beams was adjusted within a few 10^{-4} rad. Moreover, the electron and the ion beams could be centered with respect to each other within a few mm by observing the effect of the electron space charge on the ion beam velocity. This alignment was kept when passing from the pilot beam to the molecular-ion beam, as the magnetic settings of the storage ring and the electron cooler remained unchanged. The molecular-ion beam diameter, as observed with a residual-gas ionization beam-profile monitor, was limited to ≲6 mm [full width at half maximum (FWHM)] by the injection process; a slow further decrease of the ion beam diameter occurred by electron cooling with a time constant of several seconds.

B. Cross-section measurement

1. Detector setup

The detector used for the cross-section measurement was a 40×60-mm energy-sensitive Si surface-barrier detector. The energy spectrum of the neutral fragments hitting the detector is composed of several peaks; the events recorded with the full beam energy correspond to the simultaneous arrival of neutral C and H (or D for CD^+), while those recorded with $\frac{12}{13}$ ($\frac{12}{14}$ for CD) or $\frac{1}{13}$ ($\frac{2}{14}$ for CD) of the beam energy are due to the detection of a single neutral C or H (D), respectively. At low electron energy, these single neutral particles are due to the dissociation of the molecular ions in collisions with residual-gas particles in the straight section ahead of the detector (see Fig. 1). These background processes for CH^+ are

$$CH^+ + X \rightarrow C^0 + H^+ + X \tag{2}$$

or

$$CH^+ + X \rightarrow C^+ + H^0 + X, \tag{3}$$

where X denotes a residual-gas particle. Another background signal is due to electron capture from the residual-gas atoms or molecules. In this case, either a bound neutral CH (or CD) molecule is formed, or two neutral fragments are produced as in a DR reaction. These events are recorded with the same energy as a real DR event, and thus must be subtracted from the measured rate of recombination. In the present case, however, this background was negligible (as observed while the electron beam was switched off) and corrections were not needed. Moreover, at typical total count rates of $\approx3\times10^3$ s^{-1}, pulse pileup contributions to the full-energy peak were negligible.

At higher electron energy, in addition to DR, the dissociative excitation (DE) of the molecular ions is possible. Such a process leads to the formation of a neutral and a charged fragment according to

$$CH^+ + e^- \rightarrow C^0 + H^+ + e^- \tag{4}$$

or

$$CH^+ + e^- \rightarrow C^+ + H^0 + e^-. \tag{5}$$

Thus only one neutral fragment hits the Si detector and the event is not recorded under the full-energy peak. We have

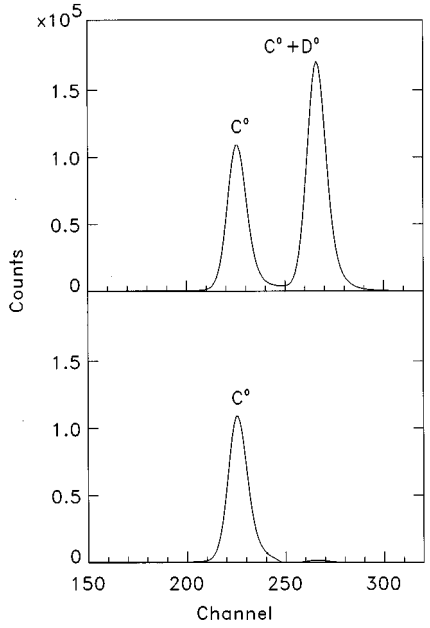

FIG. 2. Energy spectra as measured by the surface-barrier detector for the CD^+ beam of 6.6 MeV. (a) Electron cooler operation at cooling energy ($E=0$); (b) electron cooler switched off. The D^0 signal is buried in the electronic noise of the detector, which is cut off by a discriminator.

also measured DE cross sections for CH^+ and CD^+; however, those results are not included in the present paper, as they fall out of its scope. Moreover, the C^+ fragments resulting from reactions described in Eqs. (3) and (5) could be counted on a Channeltron detector located inside the closed ion orbit behind the bending magnet following the overlap region (see Fig. 1), which was installed mainly for ionization measurements on atomic ions [25].

Figure 2 shows energy spectra as measured by the surface-barrier detector for the CD^+ beam. The spectrum in Fig. 2(a) was taken with the electron cooler operating at cooling energy (i.e., $E=0$), while the spectrum shown in Fig. 2(b) was taken with the electron cooler switched off. The full-energy peak is clearly separated in Fig. 2(a) and practically nonexistent in Fig. 2(b), which indicates that the DR signal is easily separated and the background in the associated count rate is negligible. The signals of the light fragments (both for CD^+ and CH^+) could not be extracted from the electronic noise due to their low impact energy on the detector.

2. Measurement procedure and energy determination

The DR cross-section measurements were performed by recording the associated count rate in the full-energy peak of the Si detector as a function of the laboratory electron kinetic energy E_e, keeping the laboratory energy E_i of the CH^+ or CD^+ ion beams constant. After injection into the storage ring (see Sec. II A) the molecular ions first underwent electron cooling, which is caused by the friction force acting on the stored ions in the electron beam and accomplished by setting the electron energy to a value of E_c matching the nominal ion velocity in the ring.

In the longitudinal degree of freedom, the electron cooling process caused the longitudinal ion beam velocity to adjust itself to the average electron velocity in the overlap region during the cooling period of 6 s; hence the cooling electron energy and the laboratory ion energy are related by $E_c=(m_e/m_i)E_i$, where m_e and m_i denote the electron and the molecular-ion mass, respectively. The longitudinal ion velocity and its variations could be followed with high resolution by observing the Schottky noise spectrum of the stored ion beam; this spectrum also yielded the relative longitudinal velocity spread of the ion beam, which amounted to $\approx 1\times10^{-4}$ (FWHM) during the measurement.

After the electron cooling phase, the electron acceleration voltage was stepped up in order to supply a certain laboratory electron energy E_e in the overlap region. Taking into account the fact that the ion and electron beams are collinear (see Sec. II A) and that the ion velocity is determined by the cooling energy E_c as discussed above, the electron energy E in the electron-ion center-of-mass reference frame is given by

$$E=(\sqrt{E_c}-\sqrt{E_e})^2. \tag{6}$$

The electron energy E_e is found from the measured electron acceleration voltage, from which a correction is subtracted to account for the electron space-charge potential; this correction is derived from the measured electron current and the geometry of the electron beam [23] and amounts to $\approx$5% of E_e for the present parameters. By varying the energy level E_e from one injection to the next, energy scans were performed at center-of-mass (c.m.) energies E between 0.01 eV (slightly below the transverse thermal energy of the electron beam) and 40 eV; the corresponding laboratory energies E_e range between 309 and 560 eV for $E_c=302$ eV (CH^+ measurement). Positive energy differences ($E_e>E_c$) were used in order to profit from the increase of the electron density which varies $\propto E_e$ and hence almost doubles in going up to the maximum c.m. energy.

To minimize changes in the ion velocity due to the friction force caused by the electrons, the detuned electron energy was applied only for short intervals, switching the voltage back and forth between the levels corresponding to E_e and to the cooling energy E_c at a rate of 10 Hz. From the elementary theory of electron cooling [26], together with Eq. (6), the change of the c.m. energy because of the friction force is estimated for the present experimental parameters to be

$$|dE/dt| \lesssim \sqrt{E_c/E}\times 2\times10^{-5}\ \text{eV/s} \tag{7}$$

at $E \gtrsim kT_\perp$; during the modulation period it thus remained below 4×10^{-4} eV even at the lowest c.m. energies reached in the scans ($\approx$0.01 eV). This voltage ''wobbling'' also allowed us to continuously monitor the count rates at cooling energy, which were used for normalization purpose (see Sec. II B 3).

The precision of the c.m. energy scale is limited by the uncertainty of the space-charge corrected electron energies. We estimate the systematic relative uncertainty of the space-charge correction to be $\pm$5%, which yields relative errors of E_e and E_c of $\pm2\times10^{-3}$ ($\pm$0.6 eV for $E_e\approx E_c\approx300$ eV in the CH^+ measurement). The resulting systematic error of the

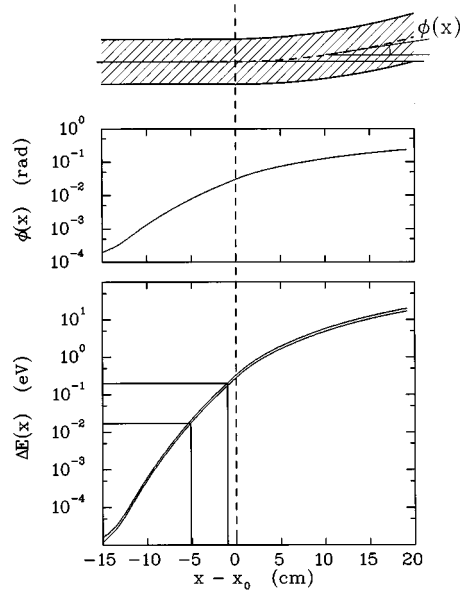

FIG. 3. The angle $\phi(s)$ between electron and ion beam and the resulting increase $\Delta E(x)$ of the c.m. energy, shown as a function of the distance $x-x_0$ from the nominal end x_0 of the straight overlap region. $\Delta E(x)$ was calculated for $E=0$ (lower curve) and $E=10$ eV (upper curve, $E_e>E_c$) at $E_c=302$ eV and includes also the effects of the space-charge potential of the electron beam ($I_e=5.5$ mA at E_c). The vertical lines indicate the limits where $\Delta E(x)$ reaches the c.m. energy spread (0.017 eV for $E\ll 0.3$ eV and 0.2 eV for $E=10$ eV).

c.m. energy scale amounts to ± 0.01 eV for $E=0.1$ eV and to ± 0.1 eV for $E=10$ eV, following an approximate scaling $\propto E^{1/2}$.

The c.m. energy distribution of the electrons [23] varies with the size of the c.m. energy itself. At low E (i.e., $E\ll kT_\perp^2/2T_\parallel \approx 0.3$ eV) the energy distribution is asymmetric and its width is limited by the transverse electron temperature (≈ 0.017 eV). In the opposite case of high E the distribution is nearly Gaussian with a width (FWHM) of $\approx 4(kT_\parallel E \ln 2)^{1/2}$ (≈ 0.2 eV for $E=10$ eV). The influence of the relative ion beam velocity spread ($\lesssim 2\times 10^{-3}$ in transverse and $\approx 1\times 10^{-4}$ in longitudinal direction) on the c.m. energy spread always remained below 10% of that stemming from the electron velocity spread. The electron space charge also caused a small variation of the longitudinal electron velocity over the ion beam cross section, the relative size of which ($\lesssim 1\times 10^{-4}$ for the present ion beam diameter) did not exceed the ion velocity spread.

The average c.m. electron energy E according to Eq. (6) is well realized over $\approx 85\%$ of the nominal overlap length $L=1.50$ m, where the angle between electron and ion beam after alignment remains below a few 10^{-4} rad. On the other hand, near the ends of the nominal overlap section and in the adjacent bending regions of the electron beam (nominal bending radius of 0.8 m, realized by toroidal magnet coils) the c.m. energy increases rapidly as the angle ϕ between the electron beam (5.0-cm diameter) and the ion beam (few mm diameter) increases. The variation of ϕ as a function of the distance $x-x_0$ from the nominal end x_0 of the overlap region, as obtained from measurements of the magnetic guiding field of the electron beam, is shown in Fig. 3 together with the resulting total increase $\Delta E(x)$ of the c.m. energy as calculated for the CH^+ measurement (including also the effect of the electron space charge). The ion beam enters (leaves) the electron beam at ≈ 18 cm from x_0. It can be seen that the increase of the c.m. energy remains below the electron energy spread considered above until ≈ -5 cm from x_0 for low E and until ≈ -1 cm from x_0 for high E (≈ 10 eV); beyond these limits, it rapidly becomes significant. Hence for narrow features in the energy dependence of the measured cross section the ''effective'' interaction length, over which the c.m. energy remains essentially unchanged, is well represented by the nominal length L. Corrections for signal contributions from the bending regions in the measured cross section will be discussed in Sec. II B 3, and possible influences of these regions on the fragment imaging in Sec. II C 2.

3. Evaluation of cross sections

The DR rate coefficient $\alpha(E)$ is derived from the measured DR count rate $r(E)$ by

$$\alpha(E)=r(E)/n_e(E)\,\eta N_i\,, \tag{8}$$

where $n_e(E)$ is the electron density at the average c.m. energy E, N_i is the number of stored ions in the ring at a given time, and $\eta=L/C$ is the ratio between the length of the interaction zone ($L=1.50$ m) and the ring circumference ($C=55.4$ m). The electron density $n_e(E)$ is deduced from the electron current $I_e(E)$, measured at the electron cooler collector, and the cross-section area S of the electron beam using the relation

$$n_e(E)=I_e(E)/Se\sqrt{2E_e/m_e}, \tag{9}$$

where e is the electron charge. The number N_i of stored ions is deduced from the ion current circulating in the ring, I_i, as

$$N_i=I_iC/qe\sqrt{2E_i/m_i}, \tag{10}$$

where qe is the ion charge. For values below 1 μA, as in the present experiment, the ion current I_i cannot be measured directly during the measurement by the current transformer of the TSR otherwise used for this purpose. Hence the rate of C^+ ions produced from the circulating CH^+ ion beam in the background reaction depicted in Eq. (3) and measured by the Channeltron detector at cooling energy during ''wobbling'' (see Sec. II B 2), was taken as a *relative* measure of the circulating ion current at any time. The C^+ rate at cooling energy offered much better statistics than the C^0 rate at cooling energy and hence was more suitable for the normalization of the spectra. It was verified that the ratio of the C^+ rate (caused by reactions with residual-gas molecules) to the C^0 rate (caused by reactions with free electrons) remained constant within $\pm 2\%$ during the energy scans; thus systematic variations of the residual-gas pressure during the energy scans had no influence on the normalization at this level of accuracy.

For the CH^+ measurement, the C^+ rate was in addition calibrated in terms of absolute ion current using a two-step procedure. First, we determined the ratio between the C^+ rate as measured by the Channeltron detector at cooling energy and the electrical signal induced by the circulating ions in a

longitudinal pickup, which was sensitively observable for an ion beam bunched by the rf cavity of the ring. Second, we calibrated the pickup signal itself using the $^{13}C^+$ pilot beam (see Sec. II B 2), which was stored under the same conditions as the CH^+ beam and was strong enough to be monitored directly by the existing current transformer. Due to the lengthy and relatively cumbersome process of calibration, we estimate the absolute value of the ion current in the CH^+ measurement to be known with an error of about $\pm 50\%$.

From the rate coefficient determined according to Eq. (8) we obtain the experimental cross section using the relation

$$\sigma(E)=\alpha(E)/\sqrt{2E/m_e}. \tag{11}$$

At energies E large compared to the c.m. energy spread (see Sec. II B 2), i.e., for $E \gtrsim 0.03$ eV, this represents the DR cross section convoluted with the experimental energy distribution.

The rate coefficient represented by Eq. (8) uses the nominal overlap length L, disregarding the recombination events taking place in the bending regions discussed above. Considering Fig. 3, these regions are expected to cause an additional signal contribution, smeared into the measured cross section at a given energy E from higher c.m. energies. Using data measured over a sufficiently large energy range, the rate coefficient $\alpha(E)$ and hence the cross section $\sigma(E)$ can be corrected for these effects, using the known variation of E_e near the ends of the overlap region and an iterative procedure described in more detail elsewhere [27]. The size of the additional signal contributions in the uncorrected spectra is typically 5–10 %, but locally reaches up to 30% as discussed in more detail in Sec. III B.

For CH^+ ions, we thus obtain an *absolute* DR cross section, while a relative DR cross section is obtained for CD^+. The absolute systematic error of the measured DR cross section is dominated by the uncertainty of the current calibration, given above. The relative uncertainties, relevant for the comparison of cross sections measured at different energies, are estimated to be $\pm 10\%$ after the correction for contributions from the bending regions.

C. Final-state branching-ratio measurement

For the DR of CH^+, we have deduced the final electronic states of the C and H fragments at various electron energies using a two-dimensional (2D) imaging system. The principle of the method is based on the fact that, when the initial state of the molecular ion is well known, a measurement of the kinetic-energy release in the dissociation yields a unique signature of the final excitation states of the fragments. In the following we will first describe the basic properties of the distribution of distances, as measured by the 2D imaging system for the diatomic molecules considered here, and the transformations needed for deducing the final excitation states from such measurements; then we will discuss details of the detection setup used in the experiment.

1. Projected-distance distributions

Consider a DR event involving an incoming electron with center-of-mass energy E, in which the two fragments C and H are released in given asymptotic excitation states such that their internal (electronic) energy, measured relative to the initial (rovibrational) energy level of the molecular ion, is E_n. The kinetic energy of relative motion, $E_{k,n}$, which is carried by the fragments is then given by energy conservation as

$$E_{k,n}=E-E_n. \tag{12}$$

The index n describes all the relevant quantum numbers needed to describe the electronic excitation of both fragments. If, prior to the dissociation, the molecular ion is moving in the laboratory frame of reference with a kinetic energy E_i ($\gg E_{k,n}$) then, after dissociation, the two fragments will start to separate from each other and move forward on a cone (see Fig. 2). On a detector set up at a distance s from the dissociation point with its plane perpendicular to the ion beam direction, the *projected* distance D between the two neutral fragments in the plane of the detector is given by energy and momentum conservation:

$$D=s\,\delta_n \sin\theta, \tag{13}$$

$$\delta_n=\frac{(m_C+m_H)}{\sqrt{m_C m_H}}\left(\frac{E_{k,n}}{E_i}\right)^{1/2}, \tag{14}$$

where θ is the angle of the molecular internuclear axis relative to the beam direction at the time when the dissociation occurs (see Fig. 2) and m_C and m_H are the fragment masses. Based on Eqs. (13) and (14), the measurement of the projected distance D is a direct measurement of the kinetic-energy release $E_{k,n}$ and, as such, also of the electronic excitation E_n of the fragments [see Eq. (12)].

Two problems complicate this measurement in comparison to the simple picture just described. First, in 2D imaging, the angle θ at which the dissociation occurs is unknown; thus a given energy release $E_{k,n}$ does not yield a fixed value of the projected distance, but a distribution of distances resulting from a statistical average over all possible dissociation angles θ. In this context, an assumption about the distribution of θ is required (see below). Second, in a heavy-ion storage ring, the molecular ions are merged with the electron beam over a relatively long distance (1.5 m at the TSR, see Fig. 2). Hence the dissociation can occur at any point along the interaction region, and the measured distribution of projected distances also represents an average over all distances s along the longitudinal extension of the interaction region.

In a previous experiment [21], where projected-distance distributions were measured for the fragments released by the DR of HD^+, it was found that anisotropies of the distribution of the dissociation angle θ can have a strong effect on the observed projected-distance distributions. For diatomic molecules, as considered here, the angular anisotropy of the fragments is simply related to the fact that the probability for DR in general depends on the angle between the internuclear axis of the molecule and the electron velocity vector (pointing along the beam direction when the transverse electron velocity can be neglected). Thus, although the internuclear axes of the stored molecules are randomly oriented, the angular distribution of the fragments resulting from a large number of DR events becomes anisotropic and reflects the angular dependence of the DR cross section. The basic properties of this angular dependence were originally predicted in

a theoretical paper by Dunn [28], based on symmetry arguments, and then further discussed in more detailed calculations by O'Malley and Taylor [29]. Although these latter calculations were aiming at the process of dissociative attachment, the same formalism basically remains valid for dissociative recombination. A suitable extension of these ideas should allow one to deduce the symmetry of the capture resonance from the observed angular dependence. Here, we limit ourselves to considering the general angular distributions consistent with the symmetry of our experimental setup.

The axial symmetry of the setup allows one to write the general angular distribution of the fragments relative to the beam direction in terms of the Legendre polynomials P_k of order k as

$$W(\theta)=\sum_{k=0}^{\infty} a_k P_k(\cos\theta), \tag{15}$$

with the normalization

$$\frac{1}{4\pi}\int W(\theta)d\Omega = a_0 = 1. \tag{16}$$

Since we do not distinguish events with angles θ and $\pi-\theta$, only the terms with even k remain in this expression. The coefficients a_k of the angular distribution depend on the formation of the capture resonance (in particular, the angular distribution of the projectile electrons in the c.m. frame and the partial waves absorbed from the continuum by the target in forming the resonance state) as well as the spins and the orbital angular momenta in the initial and final states. For simplicity, and considering that the projected-distance distributions obtained by 2D imaging are not very sensitive to the details of the angular characteristic, we restrict the analysis of the measurements to terms up to $k=2$. As we require $W(\theta)\geqslant 0$ for all θ, the condition $-1\leqslant a_2\leqslant +2$ holds for the anisotropy coefficient $a_2=0$ corresponding to an isotropic distribution. The extreme values of a_2 represent distributions of character $\sin^2\theta$ and $\cos^2\theta$, respectively [$W(\theta)=3/2\sin^2\theta$ for $a_2=-1$ and $W(\theta)=3\cos^2\theta$ for $a_2=+2$]. The distribution of projected distances for a specific final state n is then represented by

$$P_n(D)=P_{n,0}(D)+a_{n,2}P_{n,2}(D), \tag{17}$$

where $P_{n,k}(D)$ refers to the distribution for a given order k. For the isotropic component and assuming that the dissociation occurs at a fixed distance s from the detector, the projected distribution is given by

$$P_{n,0}(s,D)=\begin{cases} \dfrac{D}{\delta_n^2 s\Gamma} & \text{for } 0\leqslant D\leqslant \delta_n s \\ 0 & \text{otherwise,} \end{cases} \tag{18}$$

where

$$\Gamma=\sqrt{s^2-(D/\delta_n)^2}. \tag{19}$$

The measured distribution for an extended source and for an isotropic distribution of dissociation angles is obtained by averaging $P_{n,0}(s,D)$ over the overlap length with the electron cooler (limits s_1 and s_2, see Fig. 2), which yields the expression

$$P_{n,0}(D)=\begin{cases} \dfrac{1}{\delta_n L}\left(\arccos\dfrac{D}{\delta_n s_2}-\arccos\dfrac{D}{\delta_n s_1}\right) \\ \quad \text{for } 0\leqslant D\leqslant \delta_n s_1 \\ \dfrac{1}{\delta_n L}\arccos\dfrac{D}{\delta_n s_2} \\ \quad \text{for } \delta_n s_1\leqslant D\leqslant \delta_n s_2 \\ 0 \quad \text{otherwise,} \end{cases} \tag{20}$$

where $L=s_2-s_1$ is the interaction region length. In the present case (using the nominal straight overlap length reduced by 50 mm on either side, as discussed below) we have $s_1=5765$ mm and $s_2=7165$ mm. The index n has been added to show explicitly that $P_{n,0}(D)$ represents the distribution of projected distances for a single value of the energy release $E_{k,n}$ [see Eq. (12)], i.e., a unique set of final states for C and H in the case of CH^+. Similar normalized distribution functions can be deduced for the anisotropic component of order $k=2$,

$$P_{n,2}(D)=\begin{cases} \dfrac{1}{4\delta_n L}\left(\arccos\dfrac{D}{\delta_n s_2}-\arccos\dfrac{D}{\delta_n s_1}\right) \\ -\dfrac{3D}{4\delta_n^2 L}\left(\dfrac{\Gamma_2}{s_2^2}-\dfrac{\Gamma_1}{s_1^2}\right) \\ \quad \text{for } 0\leqslant D\leqslant \delta_n s_1 \\ \dfrac{1}{4\delta_n L}\arccos\dfrac{D}{\delta_n s_2}-\dfrac{3D}{4\delta_n^2 L}\dfrac{\Gamma_2}{s_2^2} \\ \quad \text{for } \delta_n s_1\leqslant D\leqslant \delta_n s_2 \\ 0 \quad \text{otherwise.} \end{cases}$$

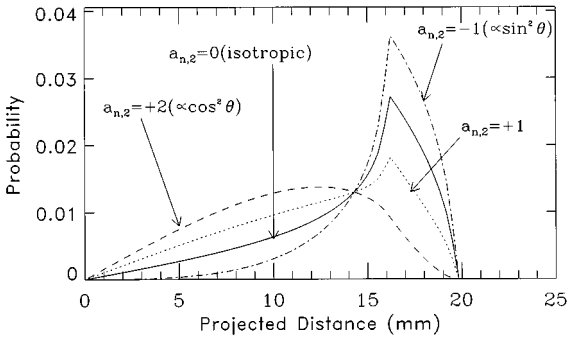

FIG. 4. Calculated shapes $P_n(D)$ of the projected-distance distribution for various initial angular anisotropies. Solid line: Isotropic distribution ($a_{n,2}=0$); dashed line: ($\cos^2\theta$)-like distribution ($a_{n,2}=2$); dot-dashed line: ($\sin^2\theta$)-like distribution ($a_{n,2}=-1$); and dotted line: $a_{n,2}=+1$. These distributions were calculated using the parameters of the present experiment for a c.m. energy release $E_{k,n}=4$ eV.

Here, the functions $\Gamma_{1,2}$ are defined by Eq. (19), setting $s=s_{1,2}$, respectively. Figure 4 shows the expected line shapes according to Eq. (17) for a few values of the anisotropy parameter $a_{2,n}$ and an energy release of 4 eV. All these

spectra rise from 0 at $D=0$ up to some maximum and then drop to 0 at $D=s_2\delta_n$. The right edge of all spectra, $D=s_2\delta_n$, corresponds to the distance between two fragments which dissociate perpendicularly to the beam direction at the largest distance (s_2) from the detector. The distributions $P_n(D)$ for $a_2 \lesssim +1$ also have a relatively sharp maximum at $D=s_1\delta_n$. The required averages over wide ranges of θ and s set a limit to the energy resolution of this technique at its present stage. However, as the lower electronic states of the C and H atoms are well separated, the resolution is, for most cases, sufficient.

Since in general more than one final state can be populated in the dissociation process, the final projected distribution is given by a sum over the different final states n according to their branching ratio:

$$P(D)=\sum_n b_n P_n(D), \tag{22}$$

where the (normalized) coefficients b_n represent the branching ratios for dissociation in a specific final state n.

Thus, in order to experimentally deduce the values of the branching ratios b_n at a given center-of-mass electron energy, it is required to measure the distribution of projected distances between the two fragments on the surface of the detector. The observed spectrum of $P(D)$ is then fitted using the function described by Eqs. (17)–(22) with $a_{n,2}$ and b_n as free parameters. It is important to point out again that, because of the projection onto two-dimensional space of a distribution which originally is three dimensional, and since the interaction region is not very small in comparison to the average distance to the detector, this fitting procedure does not constitute a detailed analysis of the angular distribution. Rather, the size of the anisotropy parameter $a_{n,2}$ gives a general characterization of the dissociation process with respect to the two extreme situations where the fragments dissociate predominantly perpendicular or parallel to the electron initial momentum (same as the beam direction if the transverse momentum of the electrons can be neglected). One should also emphasize that this imaging method, as it is sensitive to the final kinetic energy of the fragments, yields the ''true'' branching ratio of the DR process. Any radiative decay occurring after the dissociation does not influence the spectrum of projected distances. This stands in contrast to optical detection methods, where corrections for cascades between the final excited states of the fragments have to be taken into account [30,31].

2. Experimental details

For the determination of the DR final states and their corresponding branching ratios, the neutral particles were detected by an 80-mm-diam Chevron Micro-Channel-Plate (MCP), coupled to a phosphor screen (see Fig. 1). Each particle impact on the detector produced about 10^6 electrons on the output side of the MCP. These electrons were then accelerated toward the phosphor screen to create a light spot which was clearly visible. The image generated by these spots was digitized at a rate of 25 frames per second using a charge-coupled device (CCD) camera, coupled to a fast frame grabber device [32]. On analysis, the positions of the light spots were determined using a peak finding procedure, and for each frame that contains two hits their relative distance was deduced. The position resolution of the detector was ≈ 100 μm and the minimum distance which could be distinguished between two hits was ≈ 2 mm. The absolute scale of the digitized images was determined by performing defined displacements of scrapers inside the vacuum chamber, which partly blocked the particles impinging on the MCP detector.

In order for the measurement to be meaningful, only one event, defined by the time-correlated impact of a pair of C and H atoms, should be digitized per frame. To achieve this, the detector was operated in a trigger mode: Whenever an impact (i.e., at least one particle) was detected on the detector, the phosphor screen was switched off in about 20 μs by turning off the acceleration voltage between the MCP and the phosphor screen. The trigger signal indicating an impact was produced by a photomultiplier located in front of the phosphor screen, close to the CCD camera (see Fig. 1). The purpose of working in such a mode was first, as described above, to be able to handle one DR event per frame, and second, to suppress random coincidences between two unrelated single hits produced by the different background reactions in the straight section ahead of the detector [see Eqs. (2)–(5)]. The maximum time-of-flight difference for two fragments of a single CH^+ DR event is about 2–3 ns, while the average interval between two single events depends mainly on the stored beam intensity. The total rate on the detector, including products from all background reactions, was kept below 1 kHz. Thus working under the described triggering mode allowed us to achieve an excellent true-to-random coincidence ratio, which was better than 100. The typical rate of recombination events in the imaging data amounted to 0.1–10 s^{-1}. In principle, the observed projected-distance spectrum contains also events produced by electron capture from the residual gas ahead of the detector, as these events can also produce two correlated fragments. However, as mentioned above, this background was found to be negligible in the present case.

Measurements of projected-distance spectra were performed for CH^+ at zero c.m. energy ($E=0$) with continuously matched electron and ion beam velocities ($E_e=E_c$, cf. Sec. II B 2), and at selected nonzero c.m. energies. In the latter cases, for each injection and after an electron cooling phase of 6 s, the electron energy E_e was stepped up to a constant level ($E_e>E_c$), yielding the desired value of the c.m. energy E according to Eq. (6) for a measurement period of up to 20–25 s. No effort was made to apply in the imaging measurements the ''wobbling'' technique described in Sec. II B 2, which would have required a cumbersome synchronization with the CCD camera readout. However, the shift of the c.m. energy due to the friction force after 20–25 s measuring time is estimated from Eqs. (7) and (6) to be only 0.011 eV at $E=0.1$ eV (the lowest nonzero c.m. energy at which imaging measurements were performed) and thus appears tolerable; the shift, varying $\propto E^{-1/2}$, becomes even smaller for higher c.m. energy.

We finally consider the proper choice of the overlap length for fitting the projected-distance spectra, as discussed in Sec. II C 1, considering the influence of the bending regions of the electron beam (see Sec. II B 2). It can be seen from Fig. 3 that the rise of the c.m. electron energy due to

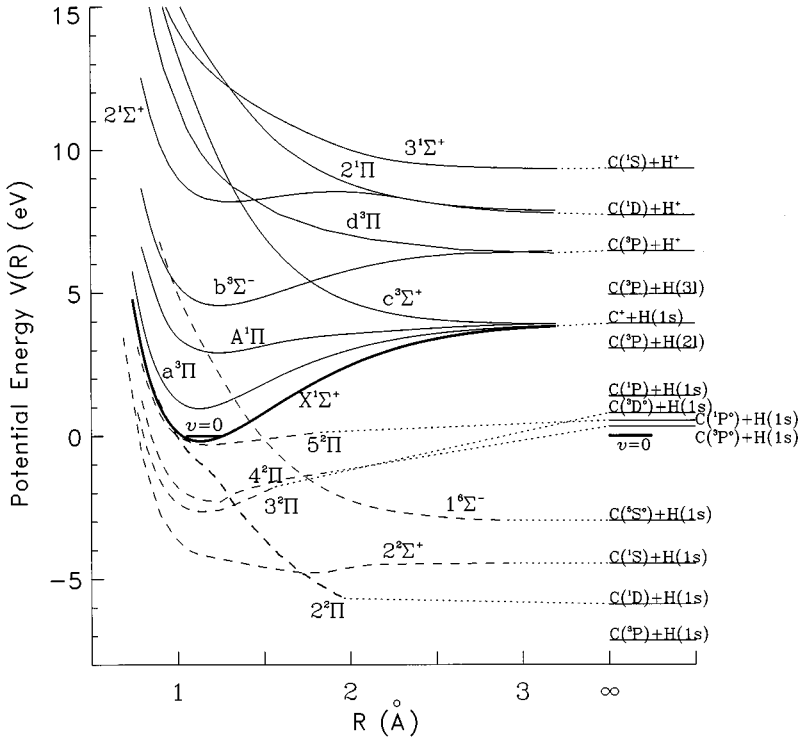

FIG. 5. Potential-energy curves for CH^+ (solid lines) and CH (dashed lines) [35,11,9]; for CH only those relevant for the DR process at $E=0$ are shown. The dotted lines show correlations between the molecular states and the separated-atom limit.

the increase of the angle between the electron and the ion beam becomes significant in comparison to the c.m. energy spread of the electrons in the straight section at -5 cm from x_0; hence for the fit we subtracted 50 mm from the nominal overlap length on either side of the electron cooler. In addition to DR events from the straight overlap region the spectra also include DR events from the overlap between electrons and ions in the bending regions, which represent an additional 18 cm on either side. Under unfavorable conditions, these events may cause significant additional contributions in the projected-distance spectra, smeared out towards higher distances corresponding to higher-energy releases $E_{k,n}$. From the discussion in Sec. III B, we see that, at the c.m. energies where fragment distributions were measured, the relative size of these contributions amounted to less than 10%, which is near the statistical uncertainty at which the branching ratios can be determined; hence it appears acceptable to disregard the influence of the bending regions.

D. Relaxation of excited states and other relevant properties of CH^+ and CD^+

In Fig. 5 we show potential-energy curves of CH^+ relevant for our experiment as well as some excited states of CH^0 [11,9,33], together with their asymptotic separated atom limits. The ground electronic state of CH^+ ($X\ ^1\Sigma^+$) is well known and has been extensively investigated [34,35]. The equilibrium bond length is $R_e=1.131$ Å and the dissociation energy is $D_0=4.08$ eV. The vibrational constant in the electronic ground state amounts to 0.344 eV. The first excited bound state is the metastable $a\ ^3\Pi$ state. This state has not been detected by spectroscopy as optical transitions to the $^1\Sigma^+$ ground state are highly forbidden, but it has been investigated theoretically [35]. The potential minimum of the $a\ ^3\Pi$ state was calculated to be about 1.14 eV above that of the $X\ ^1\Sigma^+$ state; however, the uncertainty of this value is quoted to be 0.3 eV [35]. The lifetime against radiative decay to the ground state is unknown. Above the $a\ ^3\Pi$ are the $A\ ^1\Pi$ and the $b\ ^3\Sigma^-$ states with potential minima, respectively, 3.1 and 4.8 eV higher than the $X\ ^1\Sigma^+$ level. The lifetime of the $b\ ^3\Sigma^-$ state against decay by electronic transitions to the $a\ ^3\Pi$ state has been calculated for the relevant rovibrational levels, the longest value being about 5 μs [36]. The lifetimes of the other excited electronic states of CH^+ are known to be shorter than this value [37]. Under the Born-Oppenheimer approximation and disregarding vibrational excitation, the energies as well as the lifetimes of the electronic states of CD^+ are identical to those of CH^+.

According to theoretical calculations for the lifetime of excited rovibrational levels of the $X\ ^1\Sigma^+$ state [38] the radiative lifetime for the slowest vibrational transition (from $v=1$ to 0) is 710 ms for CH^+, while it is about 4 s for CD^+. Hence it is expected that a full relaxation of the initial vibrational population produced in the ion source will occur on a time scale of $t<3$ s for CH^+ and of $t<20$ s for CD^+. However, this estimate does not include the lifetime for the radiative decay of the metastable $a\ ^3\Pi$ state. The analysis of the imaging data will show that this state is considerably populated at injection, and that the lifetime of this state, as measured in the present experiment, is about 7 s (see Sec. III A 2). Therefore in order to measure the DR cross section of fully relaxed CH^+ the data taking was started after 15 s and the beam was stored for a time of up to 20 or 25 s, after which at least 90–95 % (see Sec. III A 2) of the molecular ions have relaxed to the vibrational ground state of the $X\ ^1\Sigma^+$ state. For CD^+, the time needed to fully relax the molecular ions exceeded the useful storage time of the beam (the lifetime of the CD^+ beam in the ring has been shorter than 5 s, see Sec. II A) and consequently the results presented for this species (obtained at times of 11–14 s after injection) are only for partially relaxed ions.

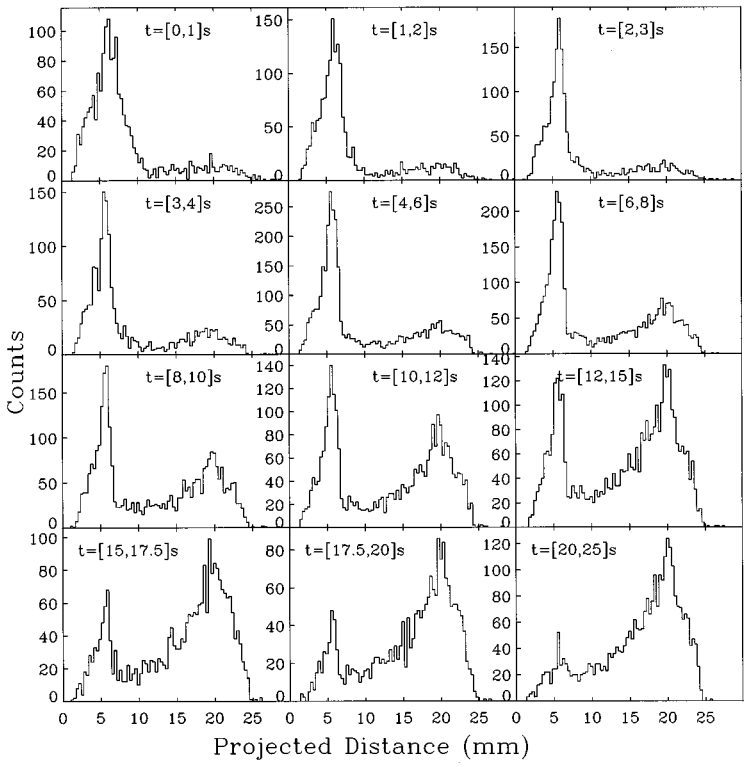

FIG. 6. Projected-distance spectrum for $E=0$ in various time slices as indicated. The left peak is due to the energy release in the DR of CH^+ ions in the $a\ ^3\Pi$ metastable state, while the right peak is for the DR of ions in the $X\ ^1\Sigma^+$ state.

III. RESULTS

A. Internal cooling of the beam in the ring

1. Time evolution of the projected-distance distribution at E =0

At $E=0$, the only asymptotic states which are energetically accessible for the recombination of vibrationally cold, ground-state CH^+ ions are those where the H atom is in its ground state, H $(1s)$, and the C atom in any of the following excited states: $C(^3P)$ ($E_{k,^3P}=7.18$ eV), $C(^1D)$ ($E_{k,^1D}=5.92$ eV), $C(^1S)$ ($E_{k,^1S}=4.50$ eV), and $C(^5S^0)$ ($E_{k,^5S}=3.00$ eV). The numbers in parentheses correspond to the kinetic-energy release for each of the final asymptotic states of the carbon atom, relative to the vibrational ground state of CH^+ [$X\ ^1\Sigma^+(v=0)$, see Fig. 5], and were obtained using the known dissociation energy D_0 of CH^+ as well as the energies of the asymptotic states of C and H [40]. Accordingly, the projected-distance distributions should correspond to high-energy releases of $\gtrsim 3$ eV.

The observed projected-distance spectrum measured for $E=0$ for various time slices after injection is shown in Fig. 6. The horizontal scale is given in mm and is the measured distance across the surface of the detector between the C and H fragments. As can be seen, two peaks are present in these spectra, with a ratio which is a strong function of the storage time. One peak, whose relative height is rising with time, corresponds to energy releases characteristic of the ground-state ions as discussed above, whereas a second peak corresponds to considerably lower-energy releases of $\lesssim 1$ eV. The fact that the branching ratio between these two is a function of time is a clear indication of internal relaxation inside the molecule. The simplest interpretation of this relaxation is related to the decay of the metastable $a\ ^3\Pi$ state.

According to the discussion in Sec. II D the radiative lifetimes for different excited bound electronic states of CH^+, apart from $a\ ^3\Pi$, amount to only $\lesssim 5\ \mu$s. The lifetime of the lowest-lying $a\ ^3\Pi$ state against decay to the ground electronic state $X\ ^1\Sigma^+$ (by spin-orbit coupling) has never been calculated or measured, but can be estimated to be of the order of a few seconds (see Sec. III A 2), which is of the same order as the decay time observed in the data of Fig. 6. Hence we come to the conclusion that the low-kinetic-energy release (small projected distance) is due to the DR of metastable, electronically excited CH^+ ions in the state $a\ ^3\Pi(v=0)$. From the time dependence of the two peaks shown in Fig. 6 and that of the cross section observed at $E=0$, it is possible to extract the lifetime of the $a\ ^3\Pi(v=0)$ level, which yields a value of $\tau_{^3\Pi}\approx 7$ s. More details will be given in Sec. III A 2. The vibrational relaxation inside the potential well of the $a\ ^3\Pi$ state can also be seen in Fig. 6, as the left peak is getting narrower during the first 3 s after injection. Vibrational excitation initially leads to a higher-energy release and thus larger projected distances, and by vibrational cooling the right-hand edge of the peak is then expected to get steeper just as observed. We can conclude that the vibrational relaxation time inside the $a\ ^3\Pi$ potential well is considerably shorter than the decay time to the ground state by electronic transitions; it is of the same order of magnitude as the vibrational relaxation time in the ground electronic state.

2. Lifetime and population of the a $^3\Pi$ state

The lifetime for the decay of the $a\ ^3\Pi$ state to the $X\ ^1\Sigma^+$ state was deduced from the measured time dependences of the total recombination rate and of the ratio between the integrated rates in the two peaks of Fig. 6, both at $E=0$. Assuming that the beam loss rates are the same for both the metastable and the ground-state ions, the total DR rate mea-

sured at a time t after injection and normalized to the circulating ion current in the ring at that time (see Sec. II B 3) is given by

$$N_{\mathrm{DR}}(t)=K[N_{a\,^3\Pi}(t)\sigma_{a\,^3\Pi}+N_{X\,^1\Sigma^+}(t)\sigma_{X\,^1\Sigma^+}], \quad (23)$$

where $N_{a\,^3\Pi}(t)$ and $N_{X\,^1\Sigma^+}(t)$ are the relative populations of CH^+ ions in the $a\,^3\Pi$ and $X\,^1\Sigma^+$ states, respectively $[N_{a\,^3\Pi}(t)+N_{X\,^1\Sigma^+}(t)=1]$, and $\sigma_{a\,^3\Pi}$ and $\sigma_{X\,^1\Sigma^+}$ are the DR cross sections from these two states at $E=0$; K is a constant of proportionality. We assume $\sigma_{a\,^3\Pi}$ and $\sigma_{X\,^1\Sigma^+}$ to be the DR cross sections for the ground vibrational levels of these states (and hence the ''effective'' DR cross sections to be constant in time, independent of vibrational relaxation). This approximation is valid in the present case, since the decay times for the vibrational levels inside the $a\,^3\Pi$ and the $X\,^1\Sigma^+$ potential wells are both considerably shorter than the decay time of $a\,^3\Pi(v=0)$ to $X\,^1\Sigma^+$, as discussed in Sec. II D.

The ratio between the two peaks observed in Fig. 6 is given by

$$R(t)=\frac{N_{X\,^1\Sigma^+}(t)\sigma_{X\,^1\Sigma^+}}{N_{a^3\Pi}(t)\sigma_{a\,^3\Pi}}. \quad (24)$$

Combining Eqs. (23) and (24), one finds that the measured functions $N_{\mathrm{DR}}(t)$ and $R(t)$ yield the following quantity proportional to the relative population of the $a\,^3\Pi$ state:

$$P_{^3\Pi}(t)=K\sigma_{a\,^3\Pi}N_{a\,^3\Pi}(t)=\frac{N_{\mathrm{DR}}(t)}{R(t)+1}. \quad (25)$$

Now, the relative population of the $a\,^3\Pi$ state should follow an exponential decay law with the natural (radiative) lifetime $\tau_{a\,^3\Pi}$; hence

$$P_{^3\Pi}(t)=P_0\exp(-t/\tau_{a\,^3\Pi}), \quad (26)$$

with an arbitrary constant P_0. Figure 7(a) shows the function $P_{^3\Pi}(t)$ as obtained from the measured data (recombination rate measurements are available for 7 s$\leqslant t\leqslant$20 s). These points were fitted using the exponential law of Eq. (26) and a value of $\tau_{a\,^3\Pi}=(7.0\pm1)$ s was obtained for the natural lifetime of the metastable $a\,^3\Pi$ state.

Based on Eq. (24), and on the exponential decay law of the relative population of the metastable $a\,^3\Pi$ state

$$N_{a\,^3\Pi}(t)=N_{a\,^3\Pi}(t_0)\exp[-(t-t_0)/\tau_{a\,^3\Pi}], \quad (27)$$

with $N_{a\,^3\Pi}(t_0)$ being the population at some arbitrary time t_0 since injection, $R(t)$ can be expressed also as

$$R(t)=\frac{\sigma_{X\,^1\Sigma^+}}{\sigma_{a\,^3\Pi}}\left[\frac{1}{N_{a\,^3\Pi}(t_0)\exp[-(t-t_0)/\tau_{a\,^3\Pi}]}-1\right]. \quad (28)$$

Figure 7(b) shows the measured function $R(t)$ together with a fit according to Eq. (28), using data points for $t>3$ s (when the initial vibrational population produced in the source is fully relaxed, see Sec. II D) and setting $\tau_{a\,^3\Pi}$ to the value of 7.0 s from the pure exponential fit discussed above. The cross-section ratio and the initial metastable population were varied in the fit and determined to be $\sigma_{X\,^1\Sigma^+}/\sigma_{a\,^3\Pi}=0.43\pm0.15$ and $N_{a\,^3\Pi}(t_0)=0.50\pm0.10$, respectively ($t_0=3$ s). This indicates that the DR cross section of the $a\,^3\Pi$ state at $E=0$ is about a factor of 2 larger than that of the ground electronic state. Now, using Eq. (27), the population of the $a\,^3\Pi$ state can be derived for all storage times t; it amounts to ≈10% at 15 s, and to ≈5% at 20 s. In other words, after 15 s, ≈90–95 % of the molecular ions have relaxed to the vibrational ground state of the $X\,^1\Sigma^+$ state. The population of the $a\,^3\Pi$ state at injection ($t=0$) can be evaluated to be ≈60–70 %.

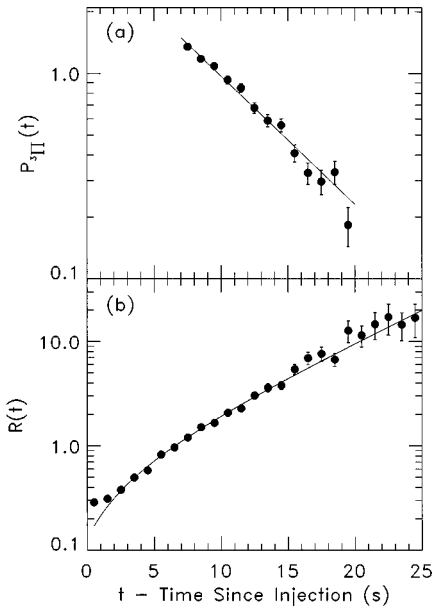

FIG. 7. Lifetime and population measurement of the $a\,^3\Pi$ state. (a) The quantity $P_{^3\Pi}(t)$, proportional to the relative population of the $a\,^3\Pi$ state according to Eq. (25), as obtained from the recombination rate and the imaging data at $E=0$, is shown versus the time since injection. The smooth line is an exponential fit. (b) The quantity $R(t)$, as obtained from the imaging data at $E=0$ according to Eq. (24), is shown versus the time since injection. The smooth line is a fit according to Eq. (28) as described in the text.

B. Experimental DR cross section

The experimental cross section for the DR of CH^+ as a function of the center-of-mass electron energy, taken in the time window of 15–20 s after injection, is shown in Fig. 8(a). As discussed above, it should reflect the cross $\sigma(E)$ from vibrationally fully relaxed CH^+ ions, of which ≳90% are in the $X\,^1\Sigma^+$ ground state and ≈5–10 % in the $a\,^3\Pi$ metastable state.

The cross section displays a rich structure with resonances both at low and high energies. We first turn to the influence of the bending regions on these data. The result before the correction for the bending regions, as discussed in Sec. II B 3, is shown as a thin line, whereas the thick line shows the cross section after this correction. The correction for the bending regions has little influence on the shape of the cross section and amounts to only a few percent; however, on the low-energy side of wide and strong resonances it becomes larger and ranges up to 30% between 4 and 8 eV. Arrows indicate the energies where final-state branching ratios were

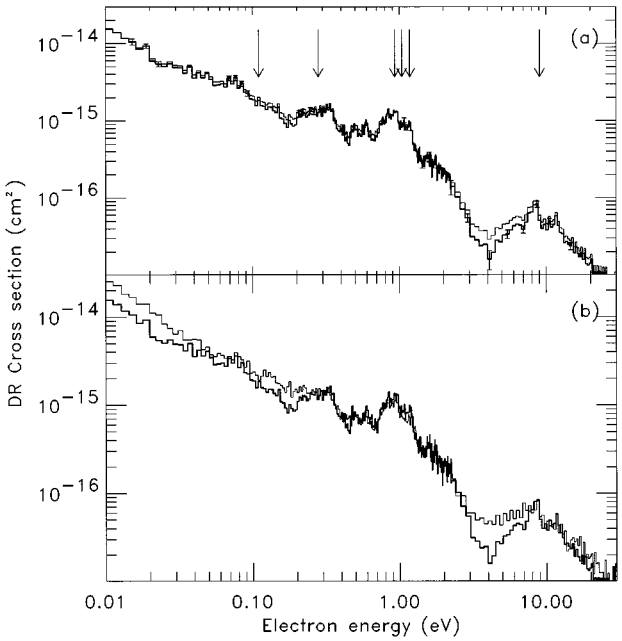

FIG. 8. (a) DR cross section of stored CH^+ ions measured 15–20 s after injection where (94±5)% of the ions are in the $X\ ^1\Sigma^+(v=0)$ state and (6±5)% are in the $a\ ^3\Pi(v=0)$ metastable state. Thick line: the experimental cross section after correction for the bending regions; thin line: result before this correction. Some typical error bars (statistical error only) are given; the systematic error of the absolute cross section is ±50%. (b) The experimental DR cross section after the correction for the bending regions. Thick line: for the time window 15–20 s after injection [shown also in (a)]; thin line: for the time window 7–10 s where (77±10)% of the ions are in the $X\ ^1\Sigma^+(v=0)$ state, and (23±10)% are in the $a\ ^3\Pi(v=0)$ metastable state.

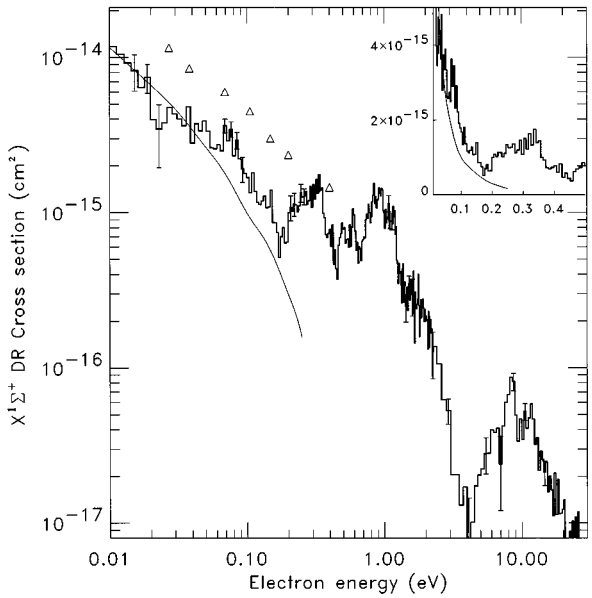

FIG. 9. DR cross section of the ground $X\ ^1\Sigma^+(v=0)$ state obtained according to the description in Sec. III B. Some typical error bars are given; the systematic error of the absolute cross section is ±50%. Also shown is the previous measurement of Mul *et al.* [14] (triangles) and the theoretical calculation by Takagi, Kosugi, and Le Dourneuf [11], convoluted with the experimental resolution (smooth line). The previous experimental data of Mul *et al.* [14] have been divided by 2 to correct for a calibration error in the original data [39]. The smooth line in the inset is also the convoluted theoretical calculation of Takagi, Kosugi, and Le Dourneuf.

measured using the imaging detector. It can be seen that the contribution from the bending regions at all these energies remains below 10%.

Figure 8(b) shows the measured DR cross sections after the correction for the bending regions for the time window of 15–20 s [thick line; same data as in Fig. 8(a)] and for the earlier time window of 7–10 s (thin line), when ≈ 25% of all ions were in the $a\ ^3\Pi$ metastable state. By combining the data measured in both these two time windows, it is possible to extract the cross section for the molecular ions in the $X\ ^1\Sigma^+$ ground state. Using the notation of the beginning of Sec. III A 2, the total DR cross section $\sigma(E,t)$ measured at time t after injection can be expressed as

$$\sigma(E,t)=N_{a\ ^3\Pi}(t)\sigma_{a\ ^3\Pi}(E)+N_{X\ ^1\Sigma^+}(t)\sigma_{X\ ^1\Sigma^+}(E). \tag{29}$$

Combining the measured cross sections from two different time windows, labeled by the median times t_1 and t_2 for which the relative populations of both states are known, yields the ground-state cross section as

$$\sigma_{X\ ^1\Sigma^+}(E)=\frac{N_{a\ ^3\Pi}(t_1)\sigma(E,t_2)-N_{a\ ^3\Pi}(t_2)\sigma(E,t_1)}{N_{a\ ^3\Pi}(t_1)-N_{a\ ^3\Pi}(t_2)} \tag{30}$$

and the metastable-state cross section as

$$\sigma_{a\ ^3\Pi}(E)=\frac{\sigma(E,t_1)-[1-N_{a\ ^3\Pi}(t_1)]\sigma_{X\ ^1\Sigma^+}(E)}{N_{a\ ^3\Pi}(t_1)}. \tag{31}$$

Thus using the two measured cross sections shown in Fig. 8(b) and the respective relative populations for the two time windows [$N_{X\ ^1\Sigma^+}(t_1)=(77\pm10)\%$ and $N_{a\ ^3\Pi}(t_1)=(23\pm10)\%$ for 7–10 s, $N_{X\ ^1\Sigma^+}(t_2)=(94\pm5)\%$ and $N_{a\ ^3\Pi}(t_2)=(6\pm5)\%$ for 15–20 s], the DR cross sections of ions in the $X\ ^1\Sigma^+$ state and of metastable $a\ ^3\Pi$ ions can be extracted separately.

For the ground-state ions this procedure yields the cross section shown in Fig. 9. The absolute value of this cross section has a systematic error of ±50% corresponding to the precision at which the ion current inside the ring could be determined (see Sec. II B 2). The previous measurements of Mul *et al.* [14] for the DR of CH^+ over the energy interval 0.03–0.4 eV are plotted for comparison as triangles. These data were obtained in a single-pass merged-beam-type experiment, using an ion source with a paramagnetic buffer gas to quench the metastable $a\ ^3\Pi$ state. The data of Mul *et al.* were divided by 2 to correct for a calibration error in the original data [39]. A theoretical calculation for the DR cross section of the $v=0$ state of ground-electronic-state CH^+ ions has been performed by Takagi, Kosugi, and Le Dourneut [11] and is shown as a smooth line in Fig. 9. The calculation, which is limited to the low-energy range $E<0.3$ eV, has been convoluted with the present energy resolution (see Sec. II B 2). Due to this convolution, all the narrow resonances caused by indirect DR, appearing as dips in the original cross section [11], are completely smeared out.

In the energy range of 0.01–0.15 eV, the overall experimental cross section of the $X\ ^1\Sigma^+$ ground state decreases as $\propto E^{-1.0}$ from an absolute value of 1.2×10^{-14} cm^{-2} at $E=0.01$ eV to 6.3×10^{-16} cm^{-2} at 0.17 eV. Superimposed on this decrease, the cross section shows a complicated structure with peaks centered at 0.080 eV (FWHM 0.040 eV) and 0.33 eV (FWHM 0.15 eV, see inset of Fig. 9), and further peaks with a FWHM of ≈0.1 eV at 0.50 and 0.59 eV. A prominent feature then appears between 0.7 and 1.2 eV (peaks at 0.96 and 1.11 eV), and finally again a smaller peak is seen at 1.55 eV. At energies above 4 eV (which is close to the dissociation energy of CH^+) the structure is dominated by two broad peaks with maxima at 8.6 and 11.7 eV. The physical interpretation and hypotheses about the nature of these low- and high-energy resonances in the DR cross section will be discussed in Sec. IV, after the presentation of the final-state branching ratios.

Compared to the previous measurement of Mul *et al.* [14,39], the experimental cross section of the $X\ ^1\Sigma^+$ state is systematically lower by a factor of ≈2. Also, the various resonances found in the present measured cross section are missing in the earlier data. The low-energy slope is comparable for both data sets, although the present cross section is a little steeper ($\propto E^{-1.0}$ vs $\propto E^{-0.9}$). The overall agreement between the present results and the theoretical calculation for $v=0$ is good up to $E=0.055$ eV. Above this energy, all the structures observed in the experimental data are not present in the theoretical cross section.

The cross section for the DR of the $a\ ^3\Pi$ metastable state could not be extracted, using the procedure described above, with reasonable relative errors. (The errors amount to 85–100 % depending on the energy.) This can be understood from the fact that, during both time windows of 7–10 and of 15–20 s, the $a\ ^3\Pi$ state was poorly populated, so that the measured cross section is largely dominated by the $X\ ^1\Sigma^+$ state. Within the errors, however, the results for the DR cross section of the $a\ ^3\Pi$ ions are at low energies consistent with the cross-section ratio of $\sigma_{X\ ^1\Sigma^+}/\sigma_{a\ ^3\Pi}=0.43\pm0.15$ derived in Sec. III A 2 for $E=0$ and, at higher energies, show a smooth decrease nearly $\propto E^{-1}$.

In Fig. 10, the cross section for the DR of CD^+ (thin line), measured with the same energy resolution as for CH^+, is compared to the DR cross section of CH^+ as measured for the time interval of 15–20 s [thick line; same data as in Fig. 8(a)]. Both cross sections have been corrected for the influence of the bending regions (see Sec. II B 3). The measuring time window for the CD^+ cross section was 11–14 s. At this point, it might be important to remember that the CD^+ ions could not be fully vibrationally relaxed (see Sec. II D). At energies above 3 eV the CD^+ cross section was extracted including also results from a previous measurement [20], where already the previous experimental energy spread was small compared to the width of the observed structures. The CD^+ cross section has been arbitrarily scaled to match the CH^+ cross section in the low-energy range, as the CD^+ ion beam current was too weak to be measured for obtaining an absolute cross section. Therefore no comparison of the overall cross-section size is possible. One finds, however, that the positions of the low-energy resonance are different and, in general, the peaks are much less pronounced. For example, the peak at ≈0.3 eV in the CH^+ cross section is missing in the CD^+ data, but a small resonance appears at 0.5 eV. On the other hand, the structure centered at 1 eV is present both for CH^+ and CD^+. The high-energy resonances for CD^+ and CH^+ are of comparable relative size and located at the same energy.

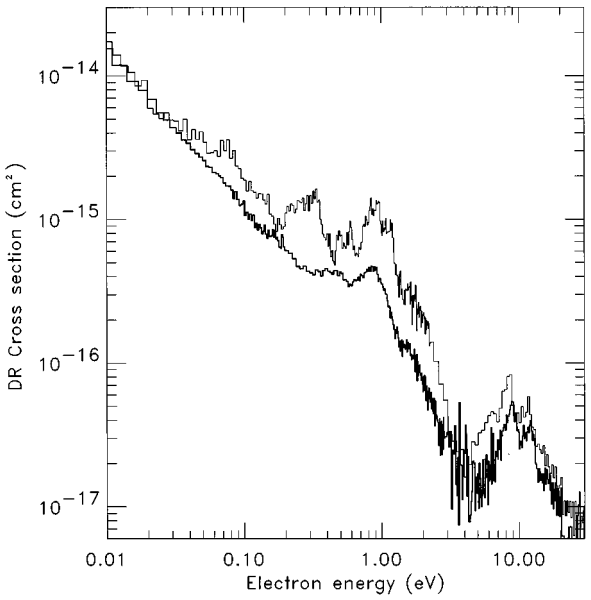

FIG. 10. DR cross section of stored, partially relaxed CD^+ ions, measured 11–14 s after injection (thick line), in comparison to the cross section of relaxed $CH^+(v=0)$ ions (15–20-s time window) of Fig. 8(a) (thin line). Both cross sections have been corrected for the influence of the bending regions. The CD^+ cross section has been arbitrarily scaled to match the CH^+ cross section at low energy.

The structures in the DR cross section (both for ground-state CH^+ and for CD^+) are probably more complex and narrower than the measured spectra reveal; some of the peaks might be smeared out by the finite energy resolution which amounts to about 0.03 eV at 1 eV; the 0.3- and 1-eV structures appear to be composed of various unresolved peaks and dips.

C. Final-state branching ratios

The branching ratios for the DR of CH^+ were measured using the 2D imaging detector as described in Sec. II C 2. Projected-distance distributions were accumulated for various electron energies, and analyzed using the functions given in Eqs. (20)–(22). The branching ratios as well as the characteristic anisotropies are summarized in Table I. We emphasize again that these anisotropies should be regarded in accordance with the limitations of the 2D imaging technique (see Sec. II C 1).

1. E=0

Figure 11(b) shows the region of large projected distances (representing high-kinetic-energy release) on an enlarged scale for the time interval $15<t<25$ s, during which the overall shape of this part of the spectrum is constant. These data represent the energy release for DR from the $X\ ^1\Sigma^+$ $(v=0)$ state of CH^+. One can clearly see from its shape that this distribution cannot be due to only a single contribution. The solid line shown on the data is the result of

TABLE I. Branching ratios b_n and anisotropy parameters $a_{n,2}$ for the DR of CH^+ as determined from the projected-distance distributions measured at different c.m. energies E. The kinetic-energy release $E_{k,n}$ was set to fixed values (as listed), except for the $a\ ^3\Pi(v=0)$ component at $E=0$.

E (eV)	Initial state	Final state n	$E_{k,n}$ (eV)	$a_{n,2}$[a]	b_n (%)
0	$a\ ^3\Pi(v=0)$	$H(1s)+C(^3P^o)$	0.90 ± 0.05[b]	0	7 ± 5
		$H(1s)+C(^1P^o)$	0.70 ± 0.05[b]	0	8^{+25}_{-8}
		$H(1s)+C(^3D^o)$	0.44 ± 0.05[b]	0	85^{+15}_{-25}
	$X\ ^1\Sigma^+(v=0)$	$H(1s)+C(^1D)$	5.92	0	79 ± 10
		$H(1s)+C(^1S)$	4.50	0	21 ± 10
0.11	$X\ ^1\Sigma^+(v=0)$	$H(1s)+C(^3P)$	7.29	$2.00^{+0}_{-1.20}$	0^{+15}_{-0}
		$H(1s)+C(^1D)$	6.03	-0.10 ± 0.75	75 ± 25
		$H(1s)+C(^1S)$	4.61	1.25 ± 0.75	25 ± 25
0.28	$X\ ^1\Sigma^+(v=0)$	$H(1s)+C(^3P)$	7.46	$2.00^{+0}_{-0.42}$	0^{+15}_{-0}
		$H(1s)+C(^1D)$	6.20	0.02 ± 0.60	75 ± 25
		$H(1s)+C(^1S)$	4.78	1.10 ± 0.45	25 ± 25
1.18[c]	$X\ ^1\Sigma^+(v=0)$	$H(1s)+C(^3P^o)$	0.88	1.55 ± 0.45	25^{+30}_{-25}
		$H(1s)+C(^1P^o)$	0.68	$1.40^{+0.60}_{-0.75}$	20^{+30}_{-20}
		$H(1s)+C(^3D^o)$	0.42	$-1.00^{+0.90}_{-0}$	45 ± 15
		$H(1s)+\{C(^1D),C(^1S)\}$	{7.10,5.68}		10 ± 7
9.04	$X\ ^1\Sigma^+(v=0)$	$H(3l)+C(^3P)$	4.13		30 ± 20
		Others			≈70

[a] $a_{n,2}=-1$: $\sin^2\theta$ character; $a_{n,2}=0$: isotropic character; $a_{n,2}=2$: $\cos^2\theta$ character.

[b] These values include a common additive term fitted to the data (see text).

[c] Measurements carried out at 0.93 and 1.04 eV have the same branching ratios and the same type of anisotropy.

a fit made using the line shape defined by Eqs. (20)–(22) for all the possible final states accessible at this energy, as listed above (see Sec. III A 1), with the branching ratios b_n being the free parameters. Since the velocity distribution of the electrons in the c.m. frame becomes isotropic in the limit $E\to0$, the anisotropy coefficients $a_{n,2}$ were first fixed to the value of 0, so that the functions $P_n(D)$ for all final states represent isotropic distributions. A fit with all $a_{n,2}$ as free parameters turns out to be compatible with isotropic angular distributions, as expected, the branching ratios remaining unchanged within the error bars. The fit results (see Table I) show that only two states are produced with significant probability, with a branching ratio of $(79\pm10)\%$ for the $H(1s)+C(^1D)$ asymptote and $(21\pm10)\%$ for the $H(1s)+C(^1S)$ asymptote. The data do not show any significant contribution from vibrational excitation in the $X\ ^1\Sigma^+$ electronic state, which justifies the use of the $v=0$ state as the initial energy level in the fits; any vibrational excitation would have been noticeable in the spectrum due to the different energy releases as demonstrated, e.g., by the first three frames of Fig. 6 for DR from the $a\ ^3\Pi$ state.

Figure 11(a) shows the left peak (small projected distances), which corresponds to energy release for DR from the $a\ ^3\Pi$ $(v=0)$ state at $E=0$, on an enlarged D scale for the time slice of $3<t<15$ s (i.e., after vibrational cooling as pointed out above), together with a fit using the theoretical distribution given by Eqs. (20)–(22). The fitted contribution from the peak at larger projected distances (see above) to this part of the spectrum has been subtracted. As expected, along the whole time slice $3<t<15$ s, the overall shape of this peak (after the subtraction) is left unchanged. The relevant branching ratios, including the corresponding energy releases, are summarized in Table I. Again, since $E=0$, at first stage the anisotropy coefficients $a_{n,2}$ were fixed to the value of 0 to represent isotropic distributions. However, as opposed to the $X\ ^1\Sigma^+$ $(v=0)$ results, their fitted values are not

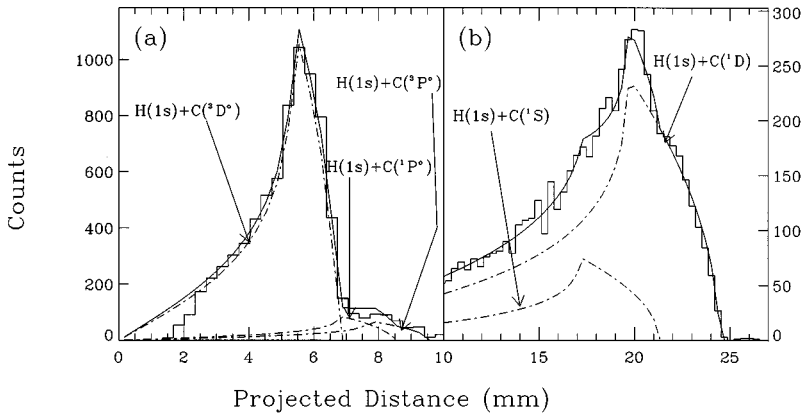

FIG. 11. Projected-distance spectrum for $E=0$ on an enlarged scale: (a) small energy release (assigned to metastable $a\ ^3\Pi$ ions), time window $3<t<15$ s (the fitted contribution from the high-D peak has been subtracted from the data); (b) large energy release (assigned to the $X\ ^1\Sigma^+$ ground state), time window $15<t<25$ s. The solid lines are least-squares fits to the distributions, as explained in the text, using the components indicated by the dot-dashed lines.

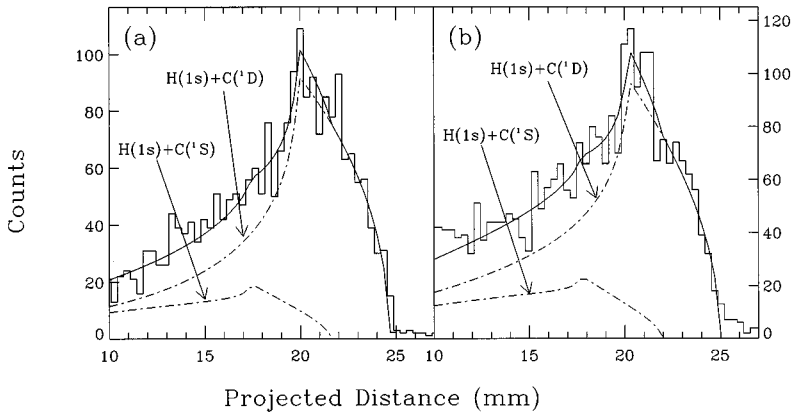

FIG. 12. Projected-distance spectrum for $E=0.11$ eV (a) and 0.28 eV (b). The solid lines are least-squares fits to the distributions, as explained in the text, using the components indicated by the dot-dashed lines.

compatible with isotropic distributions when they are introduced as free parameters, and the changes of the branching ratios in comparison to the isotropic fit exceed the error bars. An explanation for this inconsistency may be the procedure used to extract the left peak, i.e., the subtraction of the contribution from the right peak according to its fit. In any case, the branching ratios given in Table I are those obtained by requiring isotropic distributions; the error bars, however, include the results of both cases (anisotropy coefficients forced to zero or varied in the fit).

It is important to note that the value of the excitation energy of the $a\ ^3\Pi$ state is known only from theoretical calculations with large estimated uncertainty of 0.3 eV [35]. Thus in the above fit we have left the energy difference between the ground vibrational state of the $a\ ^3\Pi$ state and the $H(1s)+C(^3D^o)$ limit as a free parameter; the energy differences of the two other final states relative to the $H(1s)+C(^3D^o)$ level were fixed to their well-known values [40]. The excitation energy of the $a\ ^3\Pi(v=0)$ level relative to $X\ ^1\Sigma^+(v=0)$ is extracted from this fit to be (1.21 ± 0.05) eV, a result in good agreement with the theoretical value of (1.145 ± 0.3) eV [35,36] but having a much smaller uncertainty. This is in fact, to our best knowledge, the first measurement of this excitation energy.

2. E =0.11 and 0.28 eV

The energy of 0.28 eV was chosen in order to perform a final-state measurement on one of the large low-energy resonances in the DR cross section (see Fig. 8), while $E=0.11$ eV lies in a less structured region of the DR spectrum. Figure 12 shows the observed projected distance distributions of the carbon and hydrogen fragments for these electron energies in the ''fully relaxed'' time slice of $15<t<25$ s after injection, together with the fit results. Only the larger-distance spectrum ($D>10$ mm) is shown, as the low-distance part contains the contribution from ions in the $a\ ^3\Pi$ state, which is not relevant to the present discussion. At these two c.m. energies, the final atomic states energetically accessible from the electronic ground state are the same as for $E=0$. Fitting the measured spectra, with the branching ratios b_n and the anisotropy parameters $a_{2,n}$ being the free parameters, yields the same branching ratios for both energies (see Table I). Note that the $H(1s)+C(^3P)$ asymptote cannot be excluded as a possible final state with a small branching ratio. Now, as opposed to $E=0$, the incident electrons (seen in the c.m. frame) are strongly directed along the beam direction and the anisotropy of the DR cross section, if it exists, should become observable. The angular distributions of the main channel $H(1s)+C(^1D)$ remain consistent with an isotropic distribution of the fragments, while the other signal components show angular anisotropy, which represents dissociation in preference parallel to the beam direction. The values of the branching ratios remain unchanged (within their error bars) if the distribution is forced to be isotropic.

3. E =0.93, 1.04, and 1.18 eV

The measured projected-distance spectra for electron energies of 0.93, 1.04, and 1.18 eV, as measured between 15 and 21 s after injection, are shown in Fig. 13. For the recombination of ground-state ions, three more asymptotic states, in addition to those considered so far, have now become energetically accessible; these are $H(1s)+C(^3P^o)$, $H(1s)+C(^1P^o)$, and $H(1s)+C(^3D^o)$ (see Fig. 5). The specific values of E have been chosen in order to sample one of the most prominent structures in the DR cross section (see Fig. 8).

As can be seen from Fig. 13, the projected-distance spectra are very different from those observed at lower energies in the same time window, and correspond to much lower-kinetic-energy releases (smaller projected distances). As a consequence, the contributions of metastable- ($a\ ^3\Pi$) and ground-state ($X\ ^1\Sigma$) ions now more strongly overlap in the projected-distance spectrum; however, based on Eq. (24) and Fig. 7(b) the contribution from ions in the $a\ ^3\Pi$ state to the data shown in Fig. 13 does not exceed 15% of the integrated rate. Considering therefore the observed spectra to represent the recombination of ground-state ions, we conclude that indeed, at these electron energies, the DR fragments mainly emerge in different final states as compared to $E=0$ [see Fig. 11(b)], although there is also a long tail toward larger kinetic-energy releases (see the insets in Fig. 13).

For all three c.m. energies in this region, the fitted branching ratios are comparable within the error bars, so that the results for 1.18 eV, given in Table I, can be considered as representative. The long tail toward the larger kinetic-energy release could not be fitted because of the small statistics, but the end point of the tail clearly corresponds to the kinetic-energy release related to the $H(1s)+C(^1D)$ and $H(1s)+C(^1S)$ final states, which are the mainly populated ones at $E=0$. These tails represent a branching ratio of $\approx10\%$ at the present energies. For the $C(^3P^o)$ and $C(^1P^o)$ asymptotes, angular anisotropy toward a character of $\cos^2\theta$

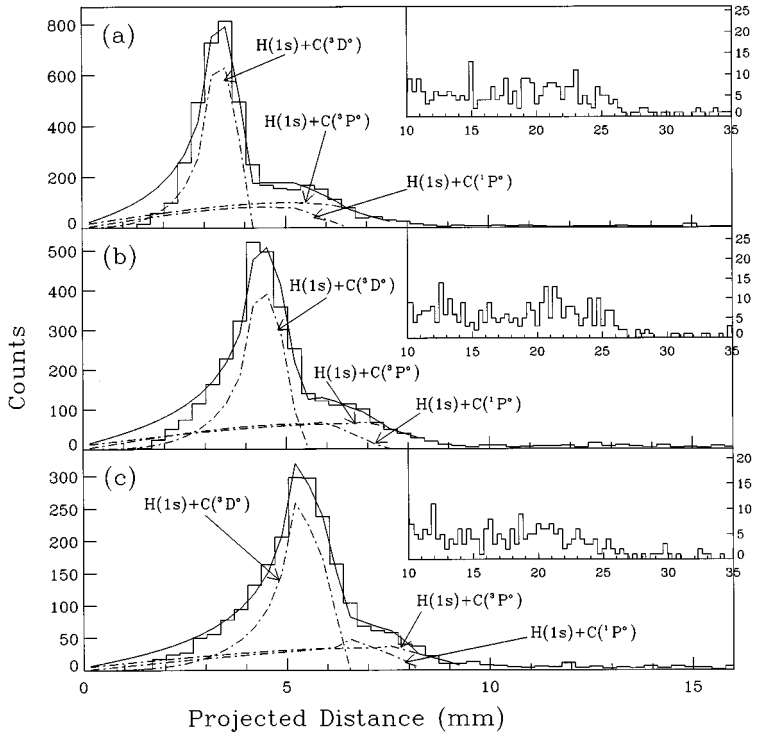

FIG. 13. Projected-distance spectra for $E=0.93$ eV (a), 1.04 eV (b), and 1.18 eV (c). The solid lines are least-squares fits to the distributions, as explained in the text, using the components indicated by the dot-dashed lines. The insets show the long-distance tails on a compressed scale.

(i.e., dissociation predominantly parallel to the beam direction) is found, whereas the character $\sin^2\theta$ (i.e., predominant dissociation perpendicular to the beam direction) is found for the $C(^3D^o)$ channel. As pointed out in Sec. II C 1, it is difficult at this point to give a more exact angular dependence, and in fact higher-order Legendre polynomials may be involved (see Sec. II C 1). This might also be the reason for the relatively poor fit at small distances in the spectra displayed in Fig. 13. The existence of the anisotropy is also supported by the fact that the spectra could not be fitted well when isotropic angular distributions were forced for all channels.

4. E =9.04 eV

As the DR rate coefficient decreases strongly as a function of energy, poor statistics makes it more difficult in this energy range to obtain reliable information on the final states. At the same time, the true-to-random coincidence ratio for the imaging detector is getting smaller due to the increase of the cross section for DE processes [Eqs. (4) and (5)]. Nevertheless, we succeeded in obtaining partial experimental results on the final states for the DR of CH^+ at $E=9.04$ eV, i.e., just on one of the high-energy resonances. The measured projected-distance distribution is shown in Fig. 14. At these energies, many states are energetically accessible, and out of them we succeeded to identify the contribution of the channel $C(^3P)+H(3l)$ with a branching ratio of $(30\pm20)\%$ (the peak position in the spectra corresponds exactly to the energy release of this channel). Due to the many possible final states, the angular distribution was difficult to determine quantitatively, but qualitatively it can be stated that it is of character between isotropic and $\sin^2\theta$. Other particular (set of) state(s), either with smaller or higher internal energies, could not be singled out, because of the smearing in the spectrum (due to the long overlap with the electron cooler and the 2D projection). The fit shown in Fig. 14 is only one out of many possible fits, and it is given only for illustration. It includes only two final states: $C(^3P)+H(3l)$ with 40% branching ratio and isotropic distribution, and $H(1s)+C(^3D^o)$ with 60% branching ratio and angular distribution of character $\cos^2\theta$.

IV. DISCUSSION

A. Lifetime of the $a\ ^3\Pi$ state

The lifetime of the $a\ ^3\Pi$ state obtained in Sec. III A 2 can be compared to a simple theoretical order-of-magnitude estimate of the radiative lifetime of this state. The finite radiative lifetime is due to the spin-orbit mixing between the $a\ ^3\Pi$ and the $A\ ^1\Pi$ states. From perturbation theory, one can obtain for the Einstein coefficient of $a\ ^3\Pi$ the following formula [41]:

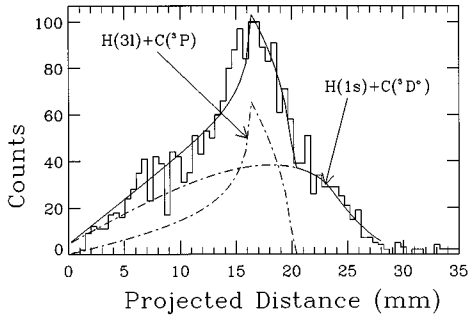

FIG. 14. Projected-distance spectrum for $E=9.04$ eV. The solid line is the fit obtained for the final channels $C(^3P)+H(3l)$ and $C(^3D^o)+H(1s)$, using the components indicated by the dot-dashed lines.

$$A(a\ ^3\Pi - X\ ^1\Sigma^+) = \left(\frac{\langle a\ ^3\Pi | H'_{so} | A\ ^1\Pi \rangle}{E(A\ ^1\Pi) - E(a\ ^3\Pi)} \right)^2 \times \left(\frac{\nu(a\ ^3\Pi - X\ ^1\Sigma^+)}{\nu(A\ ^1\Pi - X\ ^1\Sigma^+)} \right)^3 \times A(A\ ^1\Pi - X\ ^1\Sigma^+), \quad (32)$$

where $A(A\ ^1\Pi - X\ ^1\Sigma^+) = 1/\tau_{A\ ^1\Pi} = 1/(850\ \text{ns})$ [42] is the Einstein coefficient of the transition $A\ ^1\Pi - X\ ^1\Sigma^+$, $\langle a\ ^3\Pi | H'_{so} | A\ ^1\Pi \rangle \approx 30\ \text{cm}^{-1}$ is the spin-orbit interaction energy [43], $\nu(a\ ^3\Pi - X\ ^1\Sigma^+) \approx 10\,000\ \text{cm}^{-1}$ and $\nu(A\ ^1\Pi - X\ ^1\Sigma^+) \approx 25\,000\ \text{cm}^{-1}$ are the emission frequencies of the forbidden and allowed transitions, respectively, and $E(A\ ^1\Pi) - E(a\ ^3\Pi) \approx 15\,000\ \text{cm}^{-1}$ is the energy difference between the $a\ ^3\Pi$ and $A\ ^1\Pi$ states. Using these numbers in Eq. (32) we find for the lifetime of the $a\ ^3\Pi$ level in CH^+ a value of $\tau_{^3\Pi} = 1/A(a\ ^3\Pi - X\ ^1\Sigma^+) \approx 3.3$ s which, although a factor of 2 smaller than the measured value, is of the right order of magnitude. The result of this comparison should be regarded as a good agreement considering the approximations used in Eq. (32) [44].

B. DR at low energies

The theoretical DR cross section of CH^+ has been calculated by Takagi, Kosugi, and Le Dourneuf [11] up to $E = 0.3$ eV. He assumed that at these energies, the recombination proceeds via an interference between a direct process to the $2\ ^2\Pi$ dissociative state, which crosses the $X\ ^1\Sigma^+$ state close to the left turning point of the low vibrational level (see Fig. 5), and indirect processes via vibrationally excited Rydberg states converging to the $X\ ^1\Sigma^+$ state of the ion, followed by dissociation along the same $2\ ^2\Pi$ dissociative state. The $2\ ^2\Pi$ dissociative state correlates to the separate atom limit $H(1s) + C(^1D)$ which, however, according to our results, is only one of the two DR final states actually reached at $E = 0$, 0.11, and 0.28 eV (Secs. III C 1 and III C 2). The imaging data at $E = 0$ show that $(79 \pm 10)\%$ of the dissociation processes lead to the $H(1s) + C(^1D)$ asymptote and $(21 \pm 10)\%$ to the $H(1s) + C(^1S)$ asymptote, and thus seem to be in disagreement with this theoretical prediction. There are two possibilities to explain this discrepancy: (1) There may exist another state crossing the $X\ ^1\Sigma^+$ state close to the lower part of the potential curve and correlating at large distance to the $H(1s) + C(^1S)$ state, or (2) the $2\ ^2\Pi$ state may be the only one to cross the ground state of CH^+, but during the dissociation a transition occurs between the $2\ ^2\Pi$ curve and another curve which correlates to the $H(1s) + C(^1S)$ state. Our results do not allow us to differentiate between these two alternatives at this point of the argument. However, some features to be discussed below, related to the branching ratios on the 0.33-eV resonance, strongly support the second possibility.

The resonances found in the DR cross section at energies up to 0.3 eV are missing in the theoretical calculations. Since the theory already takes into account the direct process (via the $2\ ^2\Pi$ state) as well as the indirect DR processes (via Rydberg states with ground-state core), the observed resonances cannot be attributed to these mechanisms. Also, the indirect mechanism is known to yield much narrower resonances than presently measured and usually produces dips instead of peaks in the cross section. As a further experimental evidence, the imaging data show that the branching ratios for the final states over the energy range up to 0.3 eV are constant within the fitting errors (see Table I). Thus one can conclude that the recombination at these energies proceeds along the same dissociative curve(s) as at $E = 0$.

One possible interpretation of the low-energy resonances, consistent with the experimental results, is the assignment of these structures to an indirect DR process of a different type, in which the electron is first captured in one of the Rydberg states of the neutral molecule having as a core a low-lying electronically excited, bound state of CH^+. The recombination is then completed by a (pre)dissociation along one of the potential curves coupled to these Rydberg states. Such a mechanism, which we name a ''core-excited indirect DR process'' was already discussed in connection with our previous measurements of the DR of CD^+ [20] and of OH^+ [45]. The core-excited indirect process can lead to peaks in the cross section wherever the electron energy matches the energy difference between the vibrational ground state of the $X\ ^1\Sigma^+$ potential curve and a vibrational level of a Rydberg state with one of the bound excited cores. For CH^+, there are two bound excited states ($a\ ^3\Pi$ and $A\ ^1\Pi$) which can support two series of Rydberg states in this energy range. It is important to point out that capture into these Rydberg levels can occur by an electronic mechanism similar to that which controls direct recombination. Moreover, in contrast to indirect processes with a vibrationally excited core, $v = 0 \rightarrow v = 0$ capture will be possible, which has a large Franck-Condon factor and hence a large probability. Lacking theoretical calculations of the energetic positions of the Rydberg states with both the $a\ ^3\Pi$ and $A\ ^1\Pi$ cores (the position of the $a\ ^3\Pi$ state itself was known theoretically only with an uncertainty of 0.3 eV [35], and only in the present experiment was it measured directly—see Sec. III C 1), it is difficult to give a definitive answer as far as the identity of these intermediate states is concerned. However, these states must be crossed by at least the $2\ ^2\Pi$ dissociative state, as the branching-ratio measurement shows.

In fact, the observation that the branching ratios on the 0.33-eV resonance are practically the same as at lower energies strongly supports the idea that the $2\ ^2\Pi$ is the *only* state crossing both the $X\ ^1\Sigma^+$ ionic curve and the excited-core Rydberg states. The asymptotic limit $H(1s) + C(^1S)$, which is produced in $\approx 25\%$ of the recombination events, is probably populated due to a transition during the dissociation at larger internuclear distances. A good candidate for a partner in such a transition is the $2\ ^2\Sigma^+$ state, crossing the $2\ ^2\Pi$ state at 1.75 Å (see Fig. 5) and leading to $C(^1S)$ at the separate atom limit. Thus spin-orbit and rotational coupling between the $2\ ^2\Pi$ and the $^2\Sigma^+$ states would be responsible for the production of $C(^1S)$. Transitions of this type have already been studied [43], but the theoretical evaluation of the branching ratio in this specific case is beyond the scope of this work. These transitions are usually not included in present theoretical calculations of DR, which are limited to the small internuclear distances relevant to the recombination itself.

The fact that at 0.11 and 0.28 eV the $H(1s) + C(^3P)$ asymptote cannot be excluded as a final state, as it is at $E = 0$, can be explained either by the limitations that the poorer statistics of the 2D imaging spectra at $E = 0.11$ and 0.28 eV,

as compared to $E=0$, put on the analysis of the imaging data, or by the $H(1s)+C(^3P)$ asymptote being a real final state and of DR at those energies. In that case it can be reached in a similar way to the $H(1s)+C(^3P)$ asymptote, although through coupling at large internuclear distances to a different state. In any case, the above discussion and conclusions hold as they are.

At an electron energy of about 1 eV, the final-state distributions change dramatically as compared to the low-energy range. The channels $H(1s)+C(^1D)$ and $H(1s)+C(^1S)$, which were the dominant final states at low energies, now represent only 10% of the branching ratio. Instead, the most important final states at the higher energy are $H(1s)+C(^3P^o)$, $H(1s)+C(^3D^o)$, and $H(1s)+C(^1P^o)$. The dissociative curves which lead to these separate atom limits have not yet been computed theoretically, making it difficult at this point to unravel the exact pathway from the recombination point to the fragments. The simplest possibilities follow.

(1) The resonances could be due to a direct process where the electron is captured directly in one (or a few) dissociative state(s) yielding the above separated-atom limit. Because of the observed narrow width of the resonance and its complicated structure, this possibility appears quite unlikely as, in a direct process, the shape of the resonance reflects the width of the wave function in the ground state and the slope of the dissociative curve. No suitable potential curve could be found which might yield the observed spectral shape within such a scheme.

(2) An excited-core indirect process, as discussed for the lower-energy resonances, is also possible at the energies considered here. In this case, the neutral Rydberg state with excited core is predissociated by potential curves which finally lead into the $C(^3P^o)$, $C(^3D^o)$, and $C(^1P^o)$, atomic states. Although the identity of such dissociative state(s) is unknown, the $2\,^2\Pi$ state can still be dominant. Thus after its formation by electron capture and predissociation the $2\,^2\Pi$ state crosses the $3\,^2\Pi$, $4\,^2\Pi$, and $5\,^2\Pi$ Rydberg states (see Fig. 5) which correlate, at large R, to the $C(^3P^o)$, $C(^1P^o)$, and $C(^3D^o)$ states. In fact, such transitions only become possible at electron energies above $E=0.30$ eV, considering the energetic position of the lowest of these final states [i.e., $H(1s)+C(^3P^o)$].

(3) Dissociative recombination processes without curve crossing, as recently proposed by Guberman [5], are known to produce strong structures in the cross section. In such a process, a single-electron radiationless transition replaces the two-electron radiationless transition that controls the conventional direct DR (''crossing'' mode), and the DR is driven by the nuclear kinetic-energy derivative operator. More details can be found in Ref. [5].

At this point, we favor the second possibility (excited-core indirect process) on the basis that the $2\,^2\Pi$ potential curve (see Fig. 5) runs parallel to the $X\,^1\Sigma^+$ curve for electron energies from 0 up to 1 eV, so that the main dissociation channel should always remain the $2\,^2\Pi$ state.

Clearly, theoretical calculations are required in order to shed more light on the source of these resonances. Specifically, theoretical results for singly and doubly excited states of CH are required to track the ''reaction path'' from the recombination point to the final atomic fragments. Also, precise positions of the Rydberg states with $^1\Pi$ and $^3\Pi$ cores are needed for a possible assignment of the experimental resonances. On the experimental side, the angular anisotropy is difficult to interpret at the present stage as the exact functional angular dependence cannot be extracted from the 2D imaging data. On the other hand, one also has to recall that the angular dependences given by O'Malley and Taylor [Eq. (14′) in Ref. [29]] take into account only the lowest partial wave of the incident-electron wave function absorbed in forming the resonant state. For CH^+, this assumption may be in default, as it is predicted that high-order partial waves do play a role in its recombination [11]. Detailed theoretical calculations of general angular distributions for DR fragments are thus needed.

C. DR at high energies

The resonances centered at 9.05 and 12.15 eV have already been observed and explained in our previous work [20] on the DR of CD^+. They can be attributed to DR processes occurring via direct transitions to doubly excited dissociative Rydberg states of the neutral CH molecule. Resonances of this type have already been observed also in the DR of HD^+ [17] and HeH^+ [18].

The 9.05-eV resonance is likely due to an excitation to the $d\,^3\Pi$ or $c\,^3\Sigma^+$ ion cores accompanied by the capture of the incident electron in the $d\,^3\Pi(n\geqslant 3)$ or $c\,^3\Sigma^+(n\geqslant 3)$ Rydberg levels, respectively. In the imaging data, we find that one of the populated final states is $C(^3P)+H(3l)$ which at small internuclear distance correlates to the $n=3$ Rydberg states with the $d\,^3\Pi$ dissociative core (see Fig. 5). Another possibility for reaching this final state is an excitation to the $c\,^3\Sigma^+$ ion core and capture of the electron in one of the Rydberg levels of this core, followed by Landau-Zener transitions to $b\,^3\Sigma^-(n=3)$ Rydberg states which at large distance also correlate to the observed $C(^3P)+H(3l)$ atomic states. Other final states are also populated at this energy, however, as pointed out in Sec. III C 4, due to the limited resolution, a definite identification is not possible at this point.

The peak at 12.15 eV, which has also been discussed in the previous work on CD^+, is probably due to excitation and capture involving the $3\,^1\Sigma^+(nl)$ and $2\,^1\Pi(nl)$ Rydberg states with $n\geqslant 3$. However, because of the limited resolution and the low statistics of the imaging data for this c.m. energy, no data for the final states are available here. The width of these resonances reflects the Franck-Condon factor between the $X\,^1\Sigma^+(v=0)$ ground-state wave function and that of the dissociative state(s), as well as the slope of this (these) state(s) as a function of the internuclear distance.

V. CONCLUSIONS AND OUTLOOK

The DR cross sections of vibrationally cold CH^+ ions and of partially relaxed CD^+ ions were found to have many resonances which have not been predicted by theory. These resonances cannot be accounted for by the ''standard'' direct and indirect processes. We have shown that the core-excited indirect process, in which an electron is resonantly captured into a predissociating Rydberg state with an electronically excited core, is consistent with the experimental findings. The measurement of the branching ratios has provided much

additional evidence useful for the interpretation of these resonances. Moreover, it has demonstrated that, in predicting the final states of the dissociation products, not only the capture process at short internuclear distances but also the full reaction path up to large distances has to be considered. The fragment imaging spectra also yielded additional information on the molecular structure of the CH^+ ion, in particular the lifetime of the $a\ ^3\Pi(v=0)$ level, which could be determined to (7.0 ± 1) s, and the energetic position of this level relative to the $X\ ^1\Sigma^+(v=0)$ ground state, found to be (1.21 ± 0.05) eV.

The combination of merged-beam cross-section measurements and fragment imaging presented here offers a large potential for further development. More precise data on the angular characteristics of the dissociation fragments can be expected from future experiments and will call for improved theoretical descriptions of the angular dependence of the DR cross section, reflecting the influence of the incident-electron direction with respect to the internuclear axis. Further improvements of the apparatus, regarding in particular the energy resolution of the merged-beam setup and of the imaging system, are under way, and future experiments based on the use of heavy-ion storage rings and the technique of fragment imaging will then yield even more detailed information on the nature of the DR processes.

ACKNOWLEDGMENTS

We would like to thank A. Suzor-Weiner, S. Guberman, J. Tennyson, H. Lefebvre-Brion, and H. Takagi for useful discussions. This work has been partially funded by the German Federal Minister for Education, Science, Research and Technology (BMBF) under Contract No. 06HD562I(3), and by the German Israel Foundation (GIF) under Contract No. I-0208-202.07/91.

[1] *Dissociative Recombination: Theory, Experiment and Applications*, edited by J. B. A. Mitchell and S. L. Guberman (World Scientific, Singapore, 1988).
[2] A. Sternberg and A. Dalgarno, Astrophys. J. **99**, 565 (1995).
[3] G. Pineau des Forets, D. R. Flower, T. W. Hartquist, and A. Dalgarno, Mon. Not. R. Astron. Soc. **220**, 801 (1986).
[4] D. R. Bates, Phys. Rev. **78**, 492 (1950).
[5] S. L. Guberman, Phys. Rev. A **49**, 4277 (1994).
[6] J. N. Bardsley and B. R. Junker, Astrophys. J. Lett. **183**, L135 (1973).
[7] M. Krauss and P. S. Julienne, Astrophys. J. Lett. **183**, L139 (1973).
[8] A. Giusti-Suzor and H. Lefebvre-Brion, Astrophys. J. Lett. **214**, L101 (1977).
[9] E. F. van Dishoeck, J. Chem. Phys. **86**, 196 (1987).
[10] J. Tennyson, J. Phys. B **21**, 805 (1988).
[11] H. Takagi, N. Kosugi, and M. Le Dourneuf, J. Phys. B **24**, 711 (1991).
[12] A. Giusti-Suzor, J. N. Bardsley, and C. Derkits, Phys. Rev. A **28**, 682 (1983).
[13] J. B. A. Mitchell and J. Wm. McGowan, in *Physics of Ion-Ion and Electron-Ion Collisions Series B: Physics*, Vol. 83 of *NATO Advanced Study Institute, Series B: Physics*, edited by F. Brouillard and J. Wm. McGowan (Plenum, New York, 1983), p. 279.
[14] P. M. Mul *et al.*, J. Phys. B **14**, 1353 (1981).
[15] Z. Amitay, D. Zajfman, and P. Forck, Phys. Rev. A **50**, 2304 (1994).
[16] T. Heupel, Diploma thesis, University of Heidelberg, 1994 (unpublished); U. Hechtfischer *et al.* (unpublished).
[17] P. Forck *et al.*, Phys. Rev. Lett. **70**, 426 (1993).
[18] T. Tanabe *et al.*, Phys. Rev. Lett. **70**, 422 (1993).
[19] M. Larson *et al.*, Phys. Rev. Lett. **70**, 430 (1993).
[20] P. Forck *et al.*, Phys. Rev. Lett. **72**, 2002 (1994).
[21] D. Zajfman *et al.*, Phys. Rev. Lett. **75**, 814 (1995).
[22] D. Habs *et al.*, Nucl. Instrum. Methods B **43**, 390 (1989).
[23] G. Kilgus *et al.*, Phys. Rev. A **46**, 5730 (1992).
[24] S. Pastuszka *et al.*, Nucl. Instrum. Methods A **369**, 11 (1996).
[25] J. Linkemann *et al.*, Phys. Rev. Lett. **74**, 4173 (1995).
[26] H. Poth, Phys. Rep. **196**, 135 (1990).
[27] A. Lampert, A. Wolf, D. Habs, G. Kilgus, D. Schwalm, and M. Pindzola, Phys. Rev. A **53**, 1413 (1996).
[28] G. H. Dunn, Phys. Rev. Lett. **8**, 62 (1962).
[29] T. F. O'Malley and H. S. Taylor, Phys. Rev. **176**, 207 (1968).
[30] R. A. Phaneuf, D. H. Crandall, and G. H. Dunn, Phys. Rev. A **11**, 528 (1975).
[31] M. Vogler and G. H. Dunn, Phys. Rev. A **11**, 1983 (1975).
[32] D. Kella *et al.*, Nucl. Instrum. Methods A **329**, 440 (1993).
[33] H. P. D. Liu and G. Verhaegen, J. Chem. Phys. **53**, 735 (1970).
[34] H. Helm, P. C. Cosby, M. M. Graff, and J. T. Moseley, Phys. Rev. A **25**, 304 (1982).
[35] S. Green, P. S. Bagus, B. Liu, A. D. McLean, and M. Yoshimine, Phys. Rev. A **5**, 1614 (1972); R. P. Saxon, K. Kirby, and B. Liu, J. Chem. Phys. **73**, 1873 (1980); R. P. Saxon and B. Liu, *ibid*. **78**, 1344 (1983); B. Levy, J. Ridard, and E. Le Coarer, Chem. Phys. **92**, 295 (1985).
[36] I. Kusunoki, S. Sakai, S. Kato, and K. Morohuma, J. Chem. Phys. **72**, 6813 (1980).
[37] K. P. Huber and G. Herzberg, *Molecular Spectra and Molecular Structure* (Van Nostrand Reinhold Company, New York, 1979), Vol. IV, p. 144.
[38] F. R. Ornellas and F. B. C. Machado, J. Chem. Phys. **84**, 1296 (1986).
[39] J. B. A. Mitchell (private communication).
[40] S. Bashkin and J. O. Stoner, Jr., *Atomic Energy Levels and Grotrian Diagrams* (North-Holland, Amsterdam, 1975), Vol. I, p. 57.
[41] H. Lefebvre-Brion and F. Guerin, J. Chem. Phys. **49**, 1446 (1968).
[42] M. Larsson and Per E. M. Siegbahn, Chem. Phys. **76**, 175 (1983).
[43] H. Lefebvre-Brion and R. W. Field, *Perturbations in the Spectra of Diatomic Molecules* (Academic Press, London, 1986), p. 123.
[44] H. Lefebvre-Brion (private communication).
[45] Z. Amitay *et al.*, Phys. Rev. A **53**, R644 (1996).